BioGeoChemical-Argo Floats Reveal Stark Latitudinal Gradient in the Southern Ocean Deep Carbon Flux Driven by Phytoplankton Community Composition

Louis Terrats[1,2] ⓘ, Hervé Claustre[1] ⓘ, Nathan Briggs[3], Antoine Poteau[1] ⓘ, Benjamin Briat[1] ⓘ, Léo Lacour[1,4], Florian Ricour[1,5] ⓘ, Antoine Mangin[2], and Griet Neukermans[6,7]

[1]Sorbonne Université, CNRS, Laboratoire d'Océanographie de Villefranche, LOV, Villefranche-sur-Mer, France, [2]ACRI-ST, Sophia Antipolis, France, [3]National Oceanography Centre, Southampton, UK, [4]Institute for Marine and Antarctic Studies, University of Tasmania, Hobart, TAS, Australia, [5]Freshwater and Oceanic Science Unit of Research (FOCUS), University of Liège, Liège, Belgium, [6]Biology Department, Ghent University, MarSens Research Group, Ghent, Belgium, [7]Flanders Marine Institute (VLIZ), InnovOcean Campus, Ostend, Belgium

Abstract The gravitational sinking of particles in the mesopelagic layer (~200–1,000 m) transfers to the deep ocean a part of atmospheric carbon fixed by phytoplankton. This process, called the gravitational pump, exerts an important control on atmospheric CO_2 levels but remains poorly characterized given the limited spatio-temporal coverage of ship-based flux measurements. Here, we examined the gravitational pump with BioGeoChemical-Argo floats in the Southern Ocean, a critically under-sampled area. Using time-series of bio-optical measurements, we characterized the concentration of particles in the productive zone, their export and transfer efficiency in the underlying mesopelagic zone, and the magnitude of sinking flux at 1,000 m. We separated float observations into six environments delineated by latitudinal fronts, sea-ice coverage, and natural iron fertilization. Results show a significant increase in the sinking-particle flux at 1,000 m with increasing latitude, despite comparable particle concentrations in the productive layer. The variability in deep flux was driven by changes in the transfer efficiency of the flux, related to the composition of the phytoplanktonic community and the size of particles, with intense flux associated with the predominance of micro-phytoplankton and large particles at the surface. We quantified the relationships between the nature of surface particles and the flux at 1,000 m and used these results to upscale our flux survey across the whole Southern Ocean using surface observations by floats and satellites. We then estimated the basin-wide Spring-Summer flux of sinking particles at 1,000 m over the Southern Ocean (0.054 ± 0.021 Pg C).

Plain Language Summary Phytoplankton are tiny organisms that convert CO_2 to organic carbon in the sunlit layer of the ocean. A part of this carbon sinks in the form of particles and can be stored for decades to millennia in the deep ocean before returning to the atmosphere. This long-term carbon storage is important for our global climate because it moves CO_2 out of the atmosphere and into the ocean. Traditional sinking carbon measurements rely on physical collection of sinking particles using ships and moorings. These measurements can only be made sporadically and/or at very few locations. This means that it is very difficult to measure ocean carbon storage for entire oceans, leading to big uncertainty. In this study, we used autonomous underwater robots to greatly expand measurements of sinking carbon storage in the Southern Ocean. These measurements allowed us to generate a new estimate of total sinking carbon storage for the entire Southern Ocean. These measurements also uncovered clear patterns in carbon storage, which changed with season and latitude. We found that these patterns appear to be driven by particle diameter. In the springtime and closer to Antarctica, both phytoplankton and other living and dead particles grow larger, corresponding to a greater amount of carbon storage.

1. Introduction

The Biological Carbon Pump (BCP) exerts a significant control on the global climate by contributing to sequestration of atmospheric CO_2 in the ocean interior (Sarmiento & Gruber, 2006). The BCP corresponds to the downwards transport of a part of the photosynthetically produced organic material at the ocean surface that becomes ultimately sequestered when this material reaches sufficiently deep waters (>1,000 m) or the sea floor (Siegel et al., 2021). Roughly 40% of this transport is thought to be due to the cumulative actions of physical (i.e., mixed-layer pump and subduction pump) and biological mechanisms (diurnal migration pump and seasonal

migration pump) (Boyd et al., 2019). The majority (roughly 60%) of this vertical transport consists in the sinking of particles, referred to as the gravitational pump (Boyd et al., 2019). The gravitational pump is mainly governed by the following three processes: (a) the photosynthetic production of organic particles in the productive surface layer, (b) subsequent export of a fraction of these particles by sinking into the underlying mesopelagic layer ($\approx$200–1,000 m), and (c) the attenuation of the sinking flux by particle remineralization and fragmentation within the mesopelagic layer (Briggs et al., 2020; Siegel et al., 2016).

The coupling between the particle flux from the productive surface layer and the resulting flux at depth is highly dependent on the structure of the surface ocean ecosystem. The phytoplankton community composition notably determines the resulting food chains and hence the nature of particles entering in the mesopelagic domain, ranging from individual cells to aggregates and fecal pellets (Durkin et al., 2021, 2022; Legendre & Le Fèvre, 1995). The attenuation of the particle flux in the mesopelagic layer is, in turn, dependent on the nature of the sinking particles, and the phytoplankton community composition may therefore be an important driver of the gravitational pump (Durkin et al., 2021). Indeed, some studies have shown a link between the size structure of the phytoplankton community, the type of exported particles, and the transfer efficiency of the sinking flux (the proportion of the flux that survives transfer to the bottom of the mesopelagic layer) (Guidi et al., 2015; Mouw et al., 2016a). Such links suggest that particle properties in the productive layer can be potential predictors of fluxes and attenuation processes within the mesopelagic realm (e.g., Siegel et al., 2016). As surface particle properties are generally easier to observe synoptically (e.g., satellite products, reanalysis) than mesopelagic processes (essentially relying on in situ observations), they constitute a promising way to upscale the estimation of the gravitational pump to larger spatial scales. Therefore, exploring and establishing links between surface ocean variables and mesopelagic flux are required for a better estimation and prediction of the gravitational pump.

The Southern Ocean is central to climate regulation as it accounts for 40% of the oceanic uptake of anthropogenic CO_2 (DeVries, 2014), and for an estimated 30% of the global export of organic carbon to the deep ocean (Arteaga et al., 2018). Studying the gravitational pump in the Southern Ocean is challenging given the complexity of the biogeochemical environment in this area. At first order, the Southern Ocean consists of High Nutrient Low Chlorophyll (HNLC) waters where iron depletion limits the production of particles (Martin et al., 1990). In some areas however, local iron inputs from island shelves or sea ice melting disrupt the planktonic ecosystem and the resulting particle flux (Ardyna et al., 2017; Halfter et al., 2020). Additionally, the Antarctic Circumpolar Current generates permanent frontal structures that delineate zones with distinct planktonic communities. Despite this variability in the production regimes of the Southern Ocean, the spring bloom is the major biological event that structures the surface ecosystem and potentially drives the resulting carbon flux in this high-latitude environment (Rembauville, Blain, et al., 2015; Rembauville, Salter, et al., 2015; Rembauville et al., 2018; Wynn-Edwards et al., 2020). The majority of the process studies conducted so far for addressing the linkage between productive and mesopelagic layer have therefore focused on this spring period. This is for obvious scientific interest but also is due to the practical constraints of ship-based work in the rougher sea conditions of winter/fall periods. The consequence is that significant observational gaps exist, preventing to adequately characterize the gravitational pump in less productive seasons, which is nevertheless required to establish annual carbon budgets. Therefore, better understanding of the Southern Ocean's gravitational pump remains a challenge that requires an observational strategy that captures the coupled processes between the productive and mesopelagic layer over a long temporal continuum.

In this context, the BioGeoChemical-Argo (BGC-Argo) float array appears to fulfill this requirement and represents a way to develop a better understanding of the coupling between upper layer and mesopelagic processes that drive the BCP. BGC-Argo floats indeed contribute to fill some knowledge gaps by measuring bio-optical parameters at unparalleled temporal and spatial scales (Bittig et al., 2019; Claustre et al., 2020; Cornec et al., 2021). Among the core bio-optical parameters are the particulate backscattering coefficient (b_{bp}, in m^{-1}) and Chlorophyll-a fluorescence (FChl-a), proxies for the particle and Chlorophyll-a concentration respectively, enabling exploration of the underlying processes of the BCP (Briggs et al., 2011; Dall'Olmo & Mork, 2014; Lacour et al., 2019). By tracking pulses of sinking particles from the productive layer down to 1,000 m depth, BGC-Argo floats are providing breakthroughs in understanding of the gravitational pump (Briggs et al., 2020). Furthermore, when equipped with a transmissometer, BGC-Argo floats can capture the particle flux with high resolution at parking depth, typically 1,000 m (Estapa et al., 2013, 2019) and over temporal windows that capture seasonal and interannual variability. Such multi-instrumented floats thus offer the opportunity to explore the gravitational pump with unprecedented coverage.
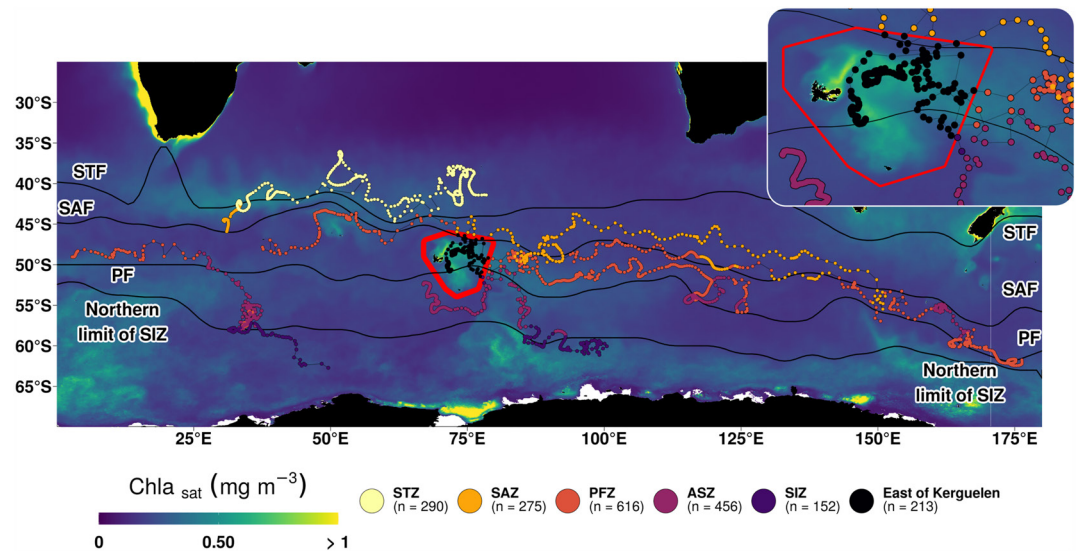
Figure 1. Sampling of the Southern Ocean by the seven floats equipped with transmissometers. Dots indicate the position of profiles. Dot colors refer to the various biophysical zones, delineated by the position of fronts and the extent of September sea-ice coverage (black lines). Fronts were located with Gray et al. (2018)'s criteria applied on climatologies of temperature (product accessible here https://doi.org/10.48670/moi-00052 and based on Guinehut et al. (2012); Mulet et al. (2012)). The boundaries of the zone called "East of Kerguelen" are drawn in red and detailed in the top right insert. The background map is the Spring-Summer climatology (2015–2019) of satellite [Chl-a] (product accessible here https://doi.org/10.48670/moi-00280 and based on Antoine and Morel (1996); Gohin et al. (2002); Hu et al. (2012); O'Reilly et al. (1998, 2000).

Furthermore, bio-optical measurements have a significant potential to characterize the nature of particles and phytoplankton assemblage at the ocean surface. For example, the ratio of b_{bp} to FChl-a has been used to characterize the dominance of diatoms (Cetinić et al., 2015) or coccolithophores (Terrats et al., 2020). More complex methods involving both environmental constraint and ratios of bio-optical measurements have been proposed to resolve the biomass of pico-, nano- and micro-phytoplankton (Rembauville et al., 2017) and high frequency measurements of b_{bp} or particulate attenuance (c_p, in m^{-1}) can be inverted to retrieve the average diameter of large particles (Briggs et al., 2013). Thanks to such developments, BGC-Argo floats have the potential to support process studies aiming at exploring and getting insights into the linkage between the structure of surface ecosystems, the resulting flux, and its attenuation in the mesopelagic domain (Claustre et al., 2021).

Process studies are ideally undertaken over longer time periods of several years, which are required to capture the variability in production regimes that drive the deep flux and hence to begin establishing annual regional budgets. Starting with deployments in 2014, seven BGC-Argo floats equipped with transmissometers have been operating in the Southern Ocean (mostly in the Indian sector), acquiring 18 annual time series of surface measurements and resulting flux. These floats provide a unique observational data set to resolve the seasonal variability in the particle flux of the different environments of Southern Ocean, and to describe the connection between the productive and mesopelagic layer in driving the gravitational pump. This paper presents an in-depth investigation of the gravitational pump in the Southern Ocean based on observations from BGC-Argo floats and satellite data. We show a clear latitudinal zonation in the intensity of the flux of sinking particles at 1,000 m and show that the size structure of the surface planktonic ecosystem drives the changes in the gravitational pump, and ultimately in the flux at 1,000 m. We finally propose surface indicators from ocean color satellite products to upscale the flux estimates at 1,000 m over the whole Southern Ocean.

2. Materials and Methods

Seven floats equipped with transmissometers were identified in the Indian sector of the Southern Ocean, which operated from 2014 to 2019 (Figure 1). The floats drifted eastward along the Antarctic Circumpolar Current, except for two floats that drifted southward and sampled waters close to Antarctica. These floats acquired sufficient data throughout the study area to capture regional and seasonal dynamics of particles from the productive layer to 1,000 m depth.

Here we present the methods related to data processing of float bio-optical measurements to obtain variables related to the concentration, nature, and flux of particles (Table 1). Briefly, we partitioned bio-optical measurements into signals from large, fast-sinking and small, slow-sinking particles. From these measurements, we identified pulses of large particles associated to the gravitational pump and computed particle export flux and transfer efficiency of particle flux in the mesopelagic layer. All the results were finally split into distinct biophysical zones based on float temperature, satellite sea-ice coverage, and natural iron fertilization.

2.1. Float Operating Procedure

The seven BGC-Argo floats operated according to cycles starting with a descent to 1,000 m, a park phase at the parking depth of 1,000 m, and an ascent to the surface during which the sensors acquired the profile data. The park phase varied from 10 days in winter to 2–3 days during the productive season. These short duration cycles of 2–3 days were required to sample the pulses of large particles with several ascending profiles (Briggs et al., 2020).

The vertical resolution of bio-optical measurements (i.e., [Chl-*a*], b_{bp}, c_p) in the top 10–50 m was always set at 1 m, allowing high-frequency sampling to derive particle diameter proxies (Briggs et al., 2013). In the mesopelagic layer, the vertical resolution of these measurements was adapted from 10 m in winter and 1 m during the productive season. This high vertical resolution in the mesopelagic layer was required to detect concentrations of large sinking particles from optical spikes with the detection method of Briggs et al. (2011) (detailed in Section 2.4), since the large particles remain rare relative to the sample volume, even within a pulse. Throughout the park phase at 1,000 m, float sensors acquired bio-optical measurements at regular intervals of either 10 or 60 min.

2.2. Float Sensors and Data Correction

The ECO Triplet (Three Channel Sensor; WET Labs, Inc., USA) measures the fluorescence of Chlorophyll-*a* (FChl-*a*) and Colored Dissolved Organic Matter (FCDOM) at excitation/emission wavelengths of 470/695 and 370/460 nm, respectively. It also measures the angular scattering coefficient of particles at 700 nm and an angle of 124°, from which we derived the particle backscattering coefficient (b_{bp} in m^{-1}) (Boss & Pegau, 2001; Schmechtig et al., 2018; Zhang et al., 2021). We corrected b_{bp}, FChl-*a*, and FCDOM profiles for out-of-range values and sensor drift over time following standard quality control procedures (Bellacicco et al., 2019; Organelli et al., 2017; Schmechtig et al., 2015). The FChl-*a* values were corrected for the Non-Photochemical Quenching (NPQ) following Xing et al. (2018) and Terrats et al. (2020), then converted to [Chl-*a*] with a float-specific coefficient estimated with daily satellite matchups of [Chl-*a*] (Terrats et al., 2020).

The C-Rover beam transmissometer (WET Labs, Inc., USA) measures the attenuation of light by particles (c_p in m^{-1}) at 660 nm along a pathlength of 25 cm, with an acceptance angle of 1.46°. The vertical position of the transmissometer causes sinking material to progressively accumulate on the detection window, resulting in a time increase in the offset of c_p profiles. We corrected the c_p profiles for this sensor drift by adjusting the profiles to an assumed b_{bp}/c_p ratio of 0.03 at 1,000 m (Terrats et al., 2020). This method is robust in the productive layer where corrected c_p values do not vary significantly with the choice of the b_{bp}/c_p ratio (Terrats et al., 2020), but is less reliable in the mesopelagic layer (see Text S1 in Supporting Information S1). We thus kept the corrected c_p values in the productive layer only, where we used them for the purposes of this study, for example, to determine the phytoplankton size-structure and the average particle size (see Section 2.7).

At the parking depth of 1,000 m, the progressive accumulation of particles on the detection window of the transmissometer caused a time-increase in c_p values throughout the park phase, which forms the basis of the so-called "optical sediment trap" (OST) technique (Estapa et al., 2013). Here, the time-increase in c_p at 1,000 m serves as a proxy for the flux of sinking particles (see Section 2.5).

We removed the deepest 50 m of each profile of [Chl-*a*], b_{bp}, and c_p values (950–1,000 m). These data often contained a very high number of spikes or unusually high values, presumably caused by particles accumulated during the park phase, on the top of the float or over the transmissometer window. Most of these accumulated particles were swept off by the vertical movement of the float during the first 50 m of the float's ascent phase (Briggs et al., 2020). We also discarded unrealistic values caused by mesopelagic organisms passing in front of the sensors. We identified these values with the method of Haëntjens et al. (2020) based on FCDOM profiles.

Table 1
List of Variables and Symbols in the Productive Layer, Mesopelagic Layer, and at 1,000 m Depth

Depth layer	Variable	Symbol	Unit	Float parameters	Equivalent "in POC" (i.e. if a c_p- or b_{bp}-to-POC coefficient is applied)	Section in the text	References
Productive layer	Chlorophyll-a concentration	[Chl-a]	mg m^{-3}	[Chl-a]		2.2	Xing et al. (2018), Terrats et al. (2020)
	Particle concentration	b_{bp}, c_p	m^{-1}	c_p, b_{bp}	mg POC m^{-3}	2.2, 2.7	Rembauville et al. (2017)
	Particle diameter	D	μm	c_p, b_{bp}		2.7	Briggs et al. (2013)
	Chl-a content per particle		pg per particle	[Chl-a]		2.7	Briggs et al. (2013)
	Proportion of each phytoplankton size class	%Micro %Nano %Pico	%	c_p, b_{bp}, [Chl-a], Temperature, Salinity		2.7	Rembauville et al. (2017)
Mesopelagic layer	Concentration of large (small) particles	$X_{l(s)}$ with X the bio-optical parameter	m^{-1} mg Chl-a m^{-3}	c_p, b_{bp} [Chl-a]	mg POC m^{-3}	2.4	Briggs et al. (2011)
	Integrated stock of large (small) particles	$iX_{l(s)}\big\|_{z_p+z_i}^{1000m}$ With X the bio-optical parameter	Unitless mg Chl-a m^{-2}	c_p, b_{bp} [Chl-a]	mg POC m^{-2}	2.6	Dall'Olmo and Mork (2014) (for small particles)
	Net flux of large (small) particles	$NF_{l(s),X}(z_p+z_i)$ with X the bio-optical parameter	day^{-1} mg Chl-a m^{-2} day^{-1}	c_p, b_{bp} [Chl-a]	mg POC m^{-2} day^{-1}	2.6	Dall'Olmo and Mork (2014) (for small particles)
	Net Transfer efficiency		%	c_p, b_{bp}, [Chl-a]		2.6	Dall'Olmo and Mork (2014) (for small particles)
	Relative abundance of large particles	%Spikes	%	c_p, b_{bp}, [Chl-a]		2.4	Rembauville et al. (2017)
1,000 m	Flux of large (small) particles at 1,000 m	$F_{l(s)}$ (1,000)	day^{-1}	c_p converted to attenuance	mg POC m^{-2} day^{-1}	2.5	Estapa et al. (2023) (for conversion to POC units)
	Spring-Summer flux of large particles at 1,000 m	F_{1SS} (1,000)			mg POC m^{-2}	3.3.2	

Note. For each variable, we indicated the unit, POC-equivalent unit, and the float parameters used to derive it. The last two columns refer to the section of the manuscript and references that describe the calculation of the variable. The symbol z_p refers to the productive depth, which is the depth of the mesopelagic layer. The symbol $z_p + z_i$ refers to a depth in the mesopelagic layer, z_i meters below z_p.

The SBE 41 CP Conductivity-Temperature-Depth sensor (Sea-bird Scientific, USA) measures the temperature, salinity and the pressure converted to depth. These data were quality controlled following Wong et al. (2022) and converted to density.

The OCR 504 radiometer (Sea-bird Scientific, USA) measures the downwelling irradiance at three wavelengths (380, 412, 490 nm) and of the light available for photosynthesis ($E_{d,\text{PAR}}$, in μW cm^{-2} nm^{-1}). We quality-controlled these measurements with the procedure of Organelli et al. (2016).

The oxygen optode 4330 (Aanderaa, Norway) senses the partial pressure of oxygen converted into oxygen concentration and was quality controlled following Thierry and Bittig (2021) (Bittig & Körtzinger, 2015; Bittig, Körtzinger, et al., 2018; Bittig, Steinhoff, et al., 2018).

2.3. Productive Depth (z_p) Determination

The so-called "productive depth" (z_p, in m) delineates the thickness of the surface layer in which particles are produced by photosynthesis, and is determined as the maximum between the Mixed Layer Depth (MLD, in m) and the euphotic depth (z_{eu}, in m) (Buesseler et al., 2020):

$$z_p = \max(\text{MLD}, z_{\text{eu}}) \tag{1}$$

We estimated the Mixed Layer Depth (MLD, in m) with the algorithm of Holte and Talley (2009) that relies on temperature, salinity, and density profiles. This method provides a more accurate estimate of the MLD in high-latitude waters than threshold and gradient approaches (Holte et al., 2017; Holte & Talley, 2009).

The euphotic depth, z_{eu}, defines the thickness of the sunlit layer that receives enough light for photosynthesis to occur. It was determined as the depth at which Photosynthetically Active Radiation (PAR) levels are 1% of PAR just below the air-water surface. Following the quality control of Organelli et al. (2016), only 47% of $E_{d,\text{PAR}}$ profiles reached the quality standards for determining z_{eu} according to its definition:

$$z_{\text{eu}} = \frac{-\ln(0.01)}{K_{d,\text{PAR}}} \tag{2}$$

With $K_{d,\text{PAR}}$ (in m^{-1}) the coefficient of diffuse attenuation of PAR at depth z equal to:

$$K_{d,\text{PAR}}(z) = \frac{-\partial \ln(E_{d,\text{PAR}}(z))}{\partial z} \tag{3}$$

Over half of $E_{d,\text{PAR}}$ profiles failed the quality-control due to perturbations in the light field explained by unstable sky conditions and the passing of clouds during the ascending profile (Organelli et al., 2016).

To compute z_{eu} for each profile, we used the global bio-optical relationship of Morel et al. (2007) that estimates K_d at 490 nm, $K_{d,490}$ (in m^{-1}), from [Chl-a] values:
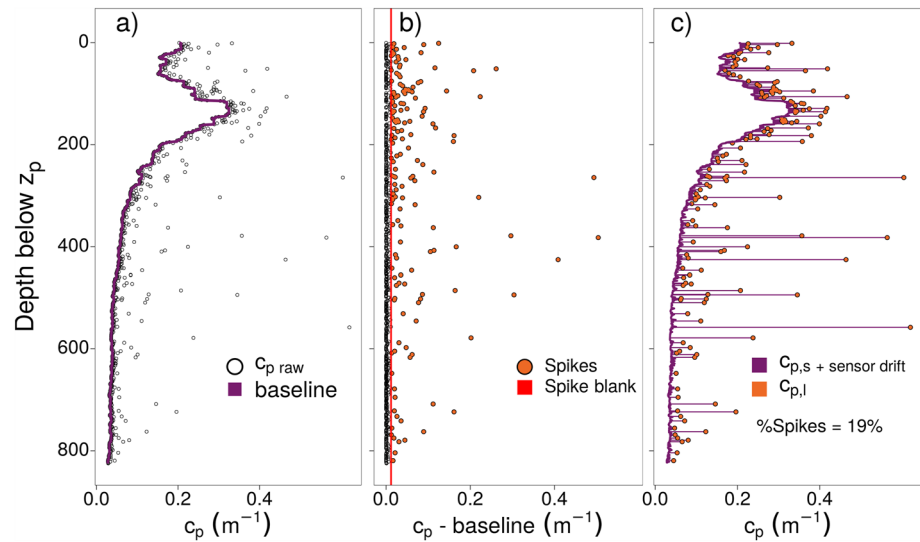
$$K_{d,490}(z) = 0.0166 + 0.08253 \, [\text{Chl}a]_{(z)}{}^{0.6259} \tag{4}$$

We then converted $K_{d,490}$ to $K_{d,\text{PAR}}$ using a regional relationship obtained by fitting the concurrent $K_{d,490}$ and $K_{d,\text{PAR}}$ values of the quality-controlled radiometric profiles (Figure S1 in Supporting Information S1):

$$K_{d,\text{PAR}}(z) = 0.002 + 1.032 \, K_{d,490}(z) \, \left(r^2 = 0.74\right) \tag{5}$$

Then, we determined z_{eu} from $K_{d,\text{PAR}}(z)$ such that:

$$\int_0^{z_{\text{eu}}} K_{d,\text{PAR}}(z) \, dz = -\ln(0.01) \tag{6}$$

Figure 2. Partitioning of a c_p profile into signal due to small and large particles (float n°6902738 on 2016-12-15). Profile (a) shows the raw measurements in the mesopelagic layer (i.e., depth below z_p computed from Equation 1) and the baseline (purple) obtained after applying the min- and max-moving filter. The residuals from the filter are shown in panel (b). Spike blank value (red line) and spike signal (orange dots) which correspond to large particles. (c) c_p profile partitioned into large (spike heights in orange) and small (purple line) particle signals. The percentage of spikes in this profile equals 19%. Note that the c_p signal from small particles also includes sensor drift.

2.4. Concentration of Particles in the Mesopelagic Layer

The particulate optical coefficients b_{bp} and c_p are commonly used as proxies for concentration in particulate organic carbon (POC concentration, [POC] in mg m^{-3}) using empirical relationships that vary widely across oceanic regions (Thomalla et al., 2017) and depth layers (Cetinić et al., 2012) due to the spatial and vertical changes in particle characteristics (e.g., size, shape, composition). Because no relationships have been reported for the mesopelagic layer in our study area, we refrained from approximating [POC] in the mesopelagic layer using a c_p- or b_{bp}-to-[POC] conversion coefficient. Instead, we assessed the pool of particles in the mesopelagic layer using the b_{bp} and c_p parameters expressed in m^{-1}, and the pool of chlorophyllous particles using [Chl-a] in mg Chl-a m^{-3}.

2.4.1. Baseline and Spikes of Bio-Optical Profiles

Bio-optical measurements in the mesopelagic layer (i.e., c_p, b_{bp}, [Chl-a]), were partitioned into signals from small and large particles according to the method of Briggs et al. (2011, 2020). The passing of large particles like fast-sinking aggregates and fecal pellets larger than approximately 100 µm causes spikes in bio-optical profiles (Briggs et al., 2020; Gardner et al., 2000) (Figure 2). Small, slow-sinking or suspended particles, on the other hand, correspond to the unspiked signal.

To partition optical signals into contributions from small and large particles, we first applied to each profile a minimum- and a maximum-moving filter with a window size adapted to the vertical resolution of sampling, that is, to 3, 7, and 11 points for profiles at 10, 2.5, and 1-m vertical resolution, respectively (Briggs et al., 2011, 2020). As such we obtained a baseline and a residual signal (Figures 2a and 2b). The baseline represents the signal from small particles, but, in the case of c_p profiles, also includes a sensor drift effect. The residuals represent the signal from large particles plus a "spike blank" estimated following Briggs et al. (2020), which equaled 1.2×10^{-4} m^{-1}, 4.6×10^{-3} m^{-1}, and 1.5×10^{-2} mg Chl-a m^{-3} for b_{bp}, c_p and [Chl-a], respectively (Figure 2b).

It is worth noting that the residuals are free of any bias caused by sensor drift, since its effect is included in the baseline signal. We can thus use the spike signal derived from c_p profiles to study large particles in the mesopelagic layer. Residuals higher than the spike blank value represent the signal from large particles (X_l, with X the bio-optical parameter, either c_p, b_{bp}, or [Chl-a]) (Figure 2b), while residuals lower than the spike blank value were added to the baseline to form the total signal from small particles (X_s, with X the bio-optical parameter) (Figure 2c). We also size-partitioned the [Chl-a] profiles to estimate [Chl-a] associated with large and small particles ([Chl-a]$_l$ and [Chl-a]$_s$).

2.4.2. Quantification of Large and Small Particles

Because the large particles that cause spikes are rare in the mesopelagic layer, accurately quantifying them can be challenging with low-sampling volumes. To gain the most accurate quantification of these particles, we relied on spike profiles measured by the c_p sensor as it benefits from a sampling volume approximately 6 times larger than the one of the b_{bp} sensor (12.5 and 1.9 mL for the transmissometer and b_{bp} sensor, respectively (Zhang et al., 2021). For quantification of the small particles, on the other hand, we used the baseline of b_{bp} profiles ($b_{bp,s}$), because the baseline of c_p profiles in the mesopelagic layer is contaminated by sensor drift.

The $b_{bp,s}$ signal is a proxy for [POC] from small particles (Briggs et al., 2011), and $c_{p,l}$ for [POC] from large particles (Briggs et al., 2011) provided that vertical resolution of the profile equaled 1 m, such as during the productive season (see Section 2.1). This high vertical resolution allows sampling of a larger volume in the mesopelagic layer that allows a more accurate quantification of large particles (Briggs et al., 2020).

The large particles can nevertheless be observed with all profiles having a vertical resolution from 1 to 10 m, but doing so comes at the cost of a lower accuracy. In our study, we extended the exploration of large particles to all profiles by deriving the percentage of spikes (%Spikes, in %), which is a proxy for the relative abundance of large particles within the entire mesopelagic layer (Rembauville et al., 2017). The spike percentage equaled the number of spikes divided by the number of measurements in the mesopelagic layer (Figure 2c), and accounted for differences in vertical resolution. The %Spikes can thus be observed throughout the year using the full set of profiles and showed significant increase consistent with the presence of intense phytoplankton blooms in the productive layer (Rembauville et al., 2017).

Here, we used %Spikes values to obtain an approximate view of the seasonal variation in the occurrence of large particles in the mesopelagic layer. For other applications requiring a more accurate quantification of large particles, such as for deriving fluxes (Section 2.6), we only used the $c_{p,l}$ profiles with a high vertical resolution (1 m).

2.5. Particle Fluxes at 1,000 m ($F_{l(s)}$(1,000 m))

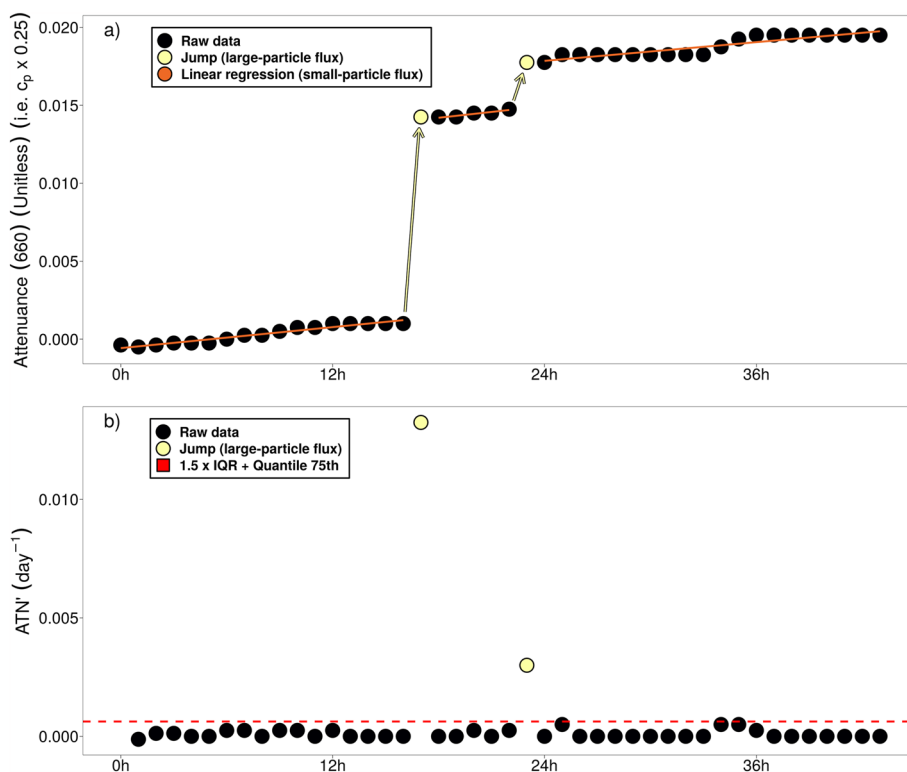### 2.5.1. Detection of Large- and Small-Particle Flux

When the transmissometer is vertically oriented, the detection window acts as an Optical Sediment Trap (OST) on which sinking material settles overtime when the float is parked at 1,000 m (Bishop & Wood, 2009; Estapa et al., 2013). The accumulation of particles leads to an increase in beam attenuance (ATN, unitless) (Figure 3), and the time derivative of ATN is a proxy for the particle flux (Estapa et al., 2017).

The flux of large and small particles was derived from the time series of ATN at 1,000 m (Estapa et al., 2013, 2017), where ATN was computed by multiplying transmissometer-derived c_p values by the pathlength of the transmissometer, 0.25 m. ATN time series were then cleared from spikes, which are attributed to the passing of active swimmers or transient particles that did not settle on the detection window (Estapa et al., 2013, 2017). To identify spikes, we computed a 7-point moving median and a 7-point moving median absolute deviation (MAD) on the ATN time-series. We identified spikes as being the residuals of the moving median above $5.2 \times$ MAD, in accordance with Leys et al. (2013). Despiked ATN time-series were then smoothed with a 7-point moving median filter. Finally, we used the temporal variation in ATN to detect the flux of small and large particles (F_s(1,000 m) and F_l(1,000 m) respectively).

When a large particle settles on the detection window, it causes a sudden and distinct increase in ATN, referred to as a "jump" (see yellow arrows on Figure 3a). Most of the jumps correspond to the settling of large particles, as suggested by Estapa et al. (2017) and supported here by the co-occurrences of jumps and b_{bp} spikes during the park phase at 1,000 m (Figure S2 in Supporting Information S1). Jumps were identified as outliers in the time series of time derivative of ATN (ATN') (Figure 3b). To achieve this, we computed the inter-quartile range (IQR) of ATN' of the time series and identified the jumps as the ATN' values higher than $1.5 \times$ IQR above the 75th Quantile (Figure 3b). This statistical technique differs from the previous methods which were either based on a fixed threshold for ATN' (Estapa et al., 2017) or on linear regression fits to ATN (Estapa et al., 2013).

We then calculated the flux of large particles by dividing the total amplitude of jumps in ATN by the duration of the park phase. Note that we also identified negative jumps as ATN' values lower than $1.5 \times$ IQR below the 25th Quantile, which account for 2.5% of our data. These negative jumps were removed from the analysis.

Figure 3. Estimation of the large- and small-particle fluxes at 1,000 m (float n°6902739 from 2016-11-19 to 2016-11-21). (a) Time series of raw attenuance (black). The yellow arrows are the jumps corresponding to the deposit of large particles. Orange lines are the linear regressions used to derive the small-particle flux. (b) Identification of jumps (yellow). Time series of ATN' (black) with the identification of jumps that correspond to an ATN' value greater than $1.5 \times$ IQR + Quantile 75th (red).

Segments of continuous and slight increase in ATN between jumps correspond to the regular settling of small particles (black points and orange lines on Figure 3a). To compute F_s(1,000 m), we linearly regressed the segments larger than 4 points, removed the segments with a negative slope, and averaged the positive slopes weighted by segment length.

2.5.2. Conversion of Attenuance Flux to POC Flux

The flux derived from ATN is expressed in units of day^{-1} and is equivalent to mg POC m^{-2} day^{-1} provided that an ATN flux-to-POC flux relationship is applied. Recently, Estapa et al. (2023) proposed a relationship based on co-located measurements of ATN flux and POC flux in diverse environments ranging from sub-tropical to sub-polar waters. However, Estapa et al. (2023) computed their ATN flux-to-POC flux relationship based on measurements between 100 and 500 m, where one can expect that the carbon-content of particles is higher than at 1,000 m where particles are more refractory. We therefore used an adjustment to the relationship of Estapa et al. (2023) that takes into account the change in POC content of sinking particles between the upper and lower mesopelagic zone. We used the ratio of POC flux to particle flux as an indicator of the relative organic carbon-content of sinking particles. We computed the POC flux to particle flux ratio between 100–500 m and at 1,000 m in the Southern Ocean from a global data compilation of sediment trap measurements (Mouw et al., 2016b). This analysis showed that the ratio decreased by a factor 2.93 between 100–500 and 1,000 m, from a POC flux/Particle flux value of 0.17 between 100 and 500 m to a value of 0.058 at 1,000 m. We thus estimated POC flux, $F_{l(s),POC}$(1,000 m) (units: mg POC m^{-2} day^{-1}), from ATN flux at 1,000 m using the ATN flux-to-POC flux relationship of Estapa et al. (2023), after adjusting for the decrease in POC content of sinking particles in the lower mesopelagic by a factor 2.93:

$$F_{l(s),POC}(1000m) = \frac{633 \times F_{l(s)}(1000m)^{0.77}}{2.93} \tag{7}$$
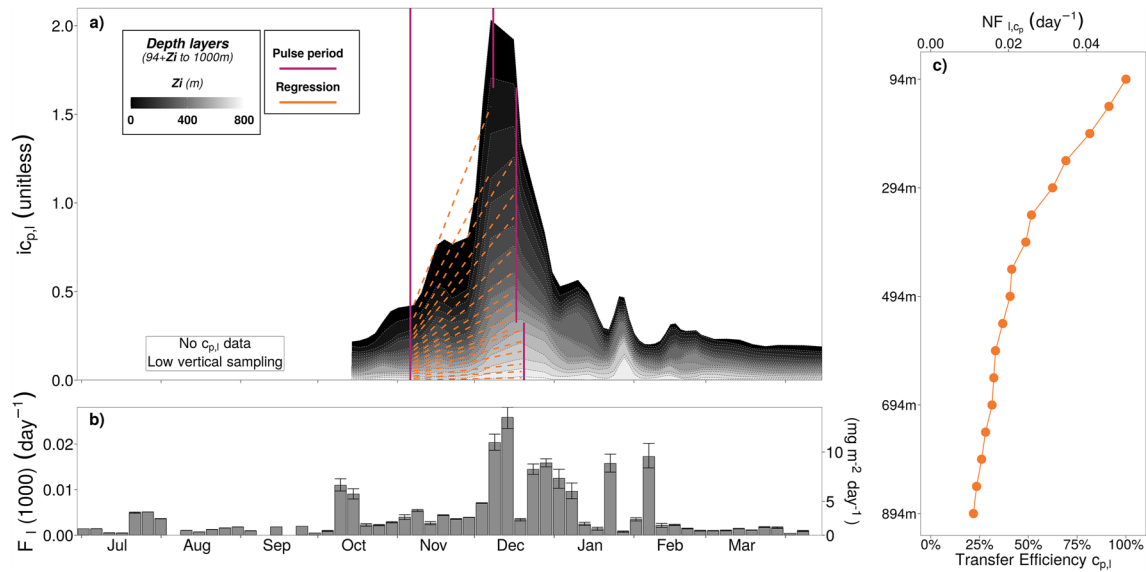
Figure 4. Example of a pulse of large particles in the mesopelagic layer obtained from float WMO n°6901583 (2016-07-01 to 2017-05-01), with time series of (a) $ic_{p,l}{}_{94+z_i}^{1000}$ for progressively deeper layers in the mesopelagic zone, (b) 1,000 m flux from the OST, (c) and profile of flux transfer efficiency. Mean zp was 94 ± 27 m.

2.6. Net Particle Flux in the Mesopelagic Layer

2.6.1. Estimation of Net Particle Flux, $NF_{l(s),X}(z_p + z_i)$

Besides estimating particle flux at 1,000 m parking depth with the OST, we also estimated particle fluxes throughout the mesopelagic layer using time series of bio-optical profiles. Following the method of Dall'Olmo and Mork ([2014](#)), we derived depth-integrated stocks of large (and small) particles, $iX_{l(s)}{}_{z_p+z_i}^{1000m}$ (dimensionless), by vertically integrating bio-optical parameters (either b_{bp}, c_p, or FChl-a) from large (and small) particles, denoted $X_{,l}$ ($X_{,s}$), over progressively deeper layers from $z_p + z_i$ to 1,000 m:

$$iX_{,l(s)}{}_{z_p+z_i}^{1000m} = \int_{z_p+z_i}^{1000} X_{,l(s)}(z)dz \tag{8}$$

with z_i ranging from 0 to 800 m. The time series of depth-integrated stocks showed pulses of particles that correspond to the seasonal accumulation of particles in the mesopelagic layer (Figure [4a](#)). These pulses correspond to a growth period in which $iX_{,l(s)}{}_{z_p+z_i}^{1000m}$ increases to reach a seasonal maximum, and were delimited between a local minimum to the seasonal maximum in $iX_{,l(s)}{}_{z_p+z_i}^{1000m}$ of each depth layer (Figure [4a](#)). Note that the starting point of the pulse was determined visually with the local minimum in $iX_{,l(s)}{}_{z_p+z_i}^{1000m}$. The sensitivity of final results to the choice of local minima is stated in Section [2.6.5](#).

Assuming mesoscale homogeneity, no lateral transport of particles and a negligible particle flux at 1,000 m (see Text S2 A–C in Supporting Information [S1](#) for further details on these assumptions), Dall'Olmo and Mork ([2014](#)) estimated the net particle flux at depth $z_p + z_i$, denoted $NF_{l(s),X}(z_p + z_i)$ (unit: day^{-1}), from the time rate of change in $iX_{,l(s)}{}_{z_p+z_i}^{1000m}$ during a pulse:

$$NF_{l(s),X}(z_p+z_i) = \frac{\partial iX_{,l(s)}{}_{z_p+z_i}^{1000}}{\partial t} \tag{9}$$

As in Dall'Olmo and Mork ([2014](#)), we calculated $NF_{l(s),X}(z_p + z_i)$ using a linear least-square regression of $iX_{,l(s)}{}_{z_p+z_i}^{1000m}$ forced through the starting point of the pulse (Figure [4a](#)).

The net flux is the result of different processes including the influx of particles at $z_p + z_i$ and the production (e.g., zooplankton fecal pellet production and production of small particles by fragmentation) and losses (consumption, loss of large particles by fragmentation) of particles in the depth layer $z_p + z_i$ to 1,000 m, as described in

Table 2
How Much Does the Flux at 1,000 m Contribute to the Calculation of the Net Flux in the Mesopelagic Layer?

Particle size	Contribution of $F_{l(s)}(1,000\text{ m})$ to $NF_{l(s),X}(z_p + z_i)$		
	Average over all z_i	At $z_i = 0$ m	At the deepest z_i
Large ($X = c_{p,l}$)	$63 \pm 25\%$	$39 \pm 21\%$	$93 \pm 14\%$ ($z_i = 800$ m)
Small ($X = b_{\mathrm{bp},s}$)	$13 \pm 7\%$	$5 \pm 2\%$	$26 \pm 8\%$ ($z_i = 700$ m)

Text S2 A in Supporting Information S1. The Net Flux calculation based on changes in integrated stocks does not include contributions to flux in steady state conditions, that is, when there is no change in $iX_{,l(s)}$ over time because particle influx equals removal rate. The net flux can nevertheless be considered as a proxy for the flux at $z_p + z_i$ under certain conditions (Dall'Olmo & Mork, 2014), such as during a pulse when accumulation rates are dominated by changes in particle influx and less by changes in particle production and loss rates.

2.6.2. When the Particle Flux at 1,000 m Is Not Negligible

We evaluated the importance of the assumption of negligible particle flux at 1,000 m by computing the contribution of $F_{l(s)}(1,000\text{ m})$ derived from the OST to $NF_{l(s),X}(z_p + z_i)$ (Table 2). On average, $F_l(1,000\text{ m})$ represented $63 \pm 25\%$ of $NF_{\mathrm{large},c_p}(z_i)$, with the lowest contribution for the shallowest z_i ($39 \pm 21\%$) and the strongest contribution for the deepest z_i ($93 \pm 14\%$). For small particles, $F_s(1,000\text{ m})$ represented $13 \pm 7\%$ of $NF_{\mathrm{small},b_{\mathrm{bp}}}(z_i)$, with the lowest contribution for the shallowest z_i ($5 \pm 2\%$) and the strongest contribution for the deepest z_i ($26 \pm 8\%$). This analysis shows that in the case of small particles, for which the method of Dall'Olmo and Mork (2014) was initially intended, the flux at 1,000 m indeed represents a small contribution, but in the case of large particles it is critical to account for non-zero particle flux at 1,000 m.

2.6.3. Accounting for Non-Zero $F_{l(s)}(1000\text{ m})$

To account for non-zero particle flux at 1,000 m depth, we modified Equation 9 as follows:

$$NF_{l(s),X}(z_p + z_i) = \frac{\partial iX_{,l(s)}{}_{z_p + z_i}^{1000}}{\partial t} + F_{l(s)}(1000\text{m}) \tag{10}$$

where $F_{l(s)}(1,000\text{ m})$ is the average of $F_{l(s)}(1,000\text{ m})$ over the duration of the pulse in units of day^{-1}. This formulation combines the methods of Dall'Olmo and Mork (2014) based on float profiles and Estapa et al. (2017) based on OST measurements at 1,000 m. This method inherently assumes that the attenuation cross sections of particles are the same whether they are in suspension or settled in a layer on the transmissometer window (i.e., they have the same c_p-to-POC ratio). While meriting some scrutiny, this assumption is supported by the following observations: (a) similar c_p-to-POC ratios between settled diatom aggregates and suspended diatoms (Estapa et al., 2017); (b) mass-specific c_p of marine aggregates are similar to those of their primary particles (Boss et al., 2009; Slade et al., 2011); and (c) mass-specific c_p is relatively insensitive to particle size variations (Neukermans et al., 2012).

We used Equation 10 to derive the net flux of large particles from $c_{p,l}$ profiles during pulses, which we identified as the most accurate proxy for [POC] from large particles (see Section 2.4.2). To derive the net flux of small particles, we relied on the $b_{\mathrm{bp},s}$ signal that is a proxy for [POC] from small particles that remains unaffected by sensor drift (see Section 2.4.2). Similarly, we addressed the flux of chlorophyllous particles using [Chl-a] profiles assuming a negligible flux of chlorophyllous particles at 1,000 m. We refer the reader to Text S2 for more details on the method and particularly the equations for estimating the net flux with each of the float parameters (Equations S5 to S8 in Supporting Information S1).

2.6.4. $NF_{l(s),X}(z_p + z_i)$ During Particle Pulses

Pulses of large particles were events lasting 32 ± 19 days on average. During these events $iX_{,l}{}_{z_p + z_i}^{1000}$ sharply increased over time, characterized by $NF_{l,c_p}(z_p)$ values ranging from 0.028 to 0.160 days^{-1} (see list of pulses on Table S3 in Supporting Information S1). We retained pulses that were tracked by floats within a quasi-Lagrangian framework as evidenced by strong similarity between successive temperature and salinity profiles (from T-S diagrams in Figure S3 in Supporting Information S1). In fact, changes in salinity and position between consecutive profiles were smaller in this study than in the study of Johnson et al. (2017) that estimated net community production within Southern Ocean water masses (Δsalinity (500 m) < 0.05, Δlongitude < 8° and Δlatitude < 5.5°). This further supports the quasi-Lagrangian tracking of the pulses by the floats in this study. Furthermore, we ruled out the effect of the mixed layer pump (Lacour et al., 2019) by constraining pulses to periods of relatively stable MLD, with standard deviation of MLD lower than 35 m. We discarded pulses with a localized increase in net flux with depth (example in Figure S4 in Supporting Information S1), which could be attributed to the

injection of particles by vertically migrating zooplankton (Buesseler & Boyd, 2009) or by the eddy-subduction pump (Llort et al., 2018). In total, we retained 17 pulses of large particles captured with spike profiles of c_p and 14 pulses of large chlorophyllous particles detected with [Chl-a] spike profiles (listed in Table S3 in Supporting Information S1).

Pulses of small, slow-sinking particles were much longer in time, and required a multi-month Lagrangian tracking that could not be achieved by individual floats in our study area. We therefore assessed small particle pulses with monthly climatologies of $iX_{s\,z_p+z_i}^{1000}$ in the different environments of the Southern Ocean (Figure S5 in Supporting Information S1), from which we derived $\mathrm{NF}_{s,X}(z_p + z_i)$ based on Equation 10 and estimates of the backscatterance flux at 1,000 m (Equation S6 in Supporting Information S1). These monthly climatologies were generally calculated using observations collected over several years, except for certain areas with lower coverage (Figure S6 in Supporting Information S1).

2.6.5. Net Transfer Efficiency

The transfer efficiency at a given depth is defined as the fraction of the particle export flux that survives transfer to that depth (Buesseler & Boyd, 2009). In this study we are however working with Net fluxes during pulses, so we defined the Net transfer efficiency at $z_i + z_p$ as follows:

$$\frac{\mathrm{NF}_{l(s),X}(z_p + z_i)}{\mathrm{NF}_{l(s),X}(z_p)} \tag{11}$$

where $\mathrm{NF}_{l(s),X}(z_p)$ is the net export flux of large (small) particles from the productive layer. The net transfer efficiency is probably a close estimate of the transfer efficiency because the net flux is considered a proxy for the flux during pulses (Dall'Olmo and Mork (2014). Based on this, we attributed the differences in net transfer efficiency to variations in the transfer efficiency of POC flux, under the assumption that profiles of c_p:POC or b_{bp}:POC ratios remain spatio-temporally uniform in the Southern Ocean. It is worth noting that estimates of the net transfer efficiency showed little sensitivity to the choice of the local minimum, varying by $10 \pm 15\%$ when the local minimum was displaced by ± 10 days.

2.7. Derived Variables in the Productive Layer

2.7.1. Particle Size Estimates

We used a multivariate regression model to estimate the proportion of different phytoplankton size classes based on bio-optical measurements and hydrological variables (Rembauville et al., 2017). The model was trained and validated in the Indian sector of the Southern Ocean, our study area. The model takes as input parameters: depth, temperature, salinity, c_p, b_{bp}, [Chl-a] and the ratios c_p/[Chl-a], b_{bp}/[Chl-a], and b_{bp}/c_p. In the present study, we reported only proportions of micro- and nano-phytoplankton (denoted %Micro and %Nano, units: %) as these groups dominated the phytoplanktonic community in this study (%Pico was always below 15%). The modeled estimates of %Micro and %Nano have an uncertainty of 17% and 19%, respectively (Rembauville et al., 2017).

We also characterized the particles in the productive layer in terms of mean diameter (D, in μm) and Chl-a-content (in pg) following the method of Briggs et al. (2013). This method calculates size parameters based on the variance-to-mean ratio of bio-optical measurements, accounting for platform motion and sensor's sampling volume (Briggs et al., 2013), for example, for size estimates with c_p:

$$D = 2\sqrt{\frac{\mathrm{var}(c_{p-d})}{\mathrm{mean}(c_p)} \frac{V}{Q_c} \frac{1}{\alpha(\tau)} \frac{1}{\pi}} \tag{12}$$

where D is the average particle diameter, $\mathrm{var}(c_{p-d})$ is the variance of the detrended c_p signal, $\mathrm{mean}(c_p)$ is the mean of the raw optical signal, V is the sample volume (12.5 mL for the C-rover), Q_c is the attenuation efficiency, which is 2 for particles much larger than the wavelength of light, and $\alpha(\tau)$ is a correction for the increase in effective sample volume due to water movement. $\alpha(\tau)$ was calculated as follows from sensor geometry and movement speed, using the sensor sample integration time of 1 s and a particle residence time of 0.1 s, derived from the mean observed float ascent speed of 10 cm s^{-1} and a mean path of 1 cm, derived from sensor geometry (Briggs et al., 2013; Rembauville et al., 2017).

Adapted to high-vertical resolution measurements, the method of Briggs et al. (2013) was applied on c_p and [Chl-a] float measurements in the productive layer where the vertical resolution was set at 1 m all year-round (e.g., Rembauville et al., 2017). It is important to note that while this mean size method has performed well in controlled laboratory conditions (relative biases in c_p-derived diameter ranging from 17% to 32%; Briggs et al., 2013) and has been found to correlate with independent phytoplankton size class designations in situ of Rembauville et al. (2017) ($r^2 = 0.62$ between D and %Micro), it has not yet been quantitatively validated in situ, where additional sources of error are expected. Independent validation should ideally be performed before results are directly quantitatively compared with size measurements from other methods. In the meantime, we expect that our estimates of D may plausibly be systematically biased by a factor of ~1.5, based on propagation of esti-mated factor of 2 uncertainty in $\alpha(\tau)$, added quadratically to a factor of 1.4 uncertainty in Q_c. Uncertainty in $\alpha(\tau)$ derives primarily from uncertainty in the horizontal component of flow through the cylindrical sample volume of a vertically oriented profiling C-rover, which impacts path length and residence time. Uncertainty in Q_c derives from the optical properties of the particle population.

2.7.2. Particle and Nutrient Concentrations

The bulk concentration of particles in the productive layer was obtained by smoothing the bio-optical profiles with a median and mean moving filter (Briggs et al., 2011). We estimated the corresponding carbon concentration by converting b_{bp} into POC concentration with the relationship of Rembauville et al. (2017) determined from samples in the surface waters of the Indian sector of the Southern Ocean (i.e., [POC] (mg C m^{-3}) = (3963.45 b_{bp}–0.6) × 12, $r^2 = 0.9$).

Concentrations in macronutrients, such as nitrate ([NO$_3^-$], in μmol kg^{-1}) and silicate ([Si(OH)$_4$], in μmol kg^{-1}), were derived using the CANYON-B neural network (Bittig, Körtzinger, et al., 2018; Bittig, Steinhoff, et al., 2018; Sauzède et al., 2017) based on hydrological and oxygen data. The global accuracy of [Si(OH)$_4$] and [NO$_3^-$] is 2.3 μmol kg^{-1} and 0.68 μmol kg^{-1}, respectively (Bittig, Körtzinger, et al., 2018; Bittig, Steinhoff, et al., 2018).

2.8. Delimitation of Southern Ocean Zones

We split the Southern Ocean into different zones delineated by fronts and the seasonal presence of sea ice (Figure 1). We used float temperature and satellite sea-ice coverage to delineate the following zones from north to south (Gray et al., 2018): the Sub-Tropical Zone (STZ), Sub-Antarctic Zone (SAZ), Polar Frontal Zone (PFZ), Antarctic-Southern Zone (ASZ), and the Seasonal-Ice Zone (SIZ). The STZ and SAZ were separated by the Sub-Tropical Front (STF), SAZ and PFZ by the Sub-Antarctic Front (SAF), PFZ and ASZ by the Polar Front (PF), and the ASZ and SIZ by a limit of 15% of sea-ice coverage in September (Gray et al., 2018). These five zones were mainly composed of iron-limited HNLC waters. We further identified a sixth zone East of the Kerguelen Plateau, an area with natural iron input that increases the production of particles and potentially impacts the resulting fluxes (Blain et al., 2007). We identified this zone using a threshold of 0.75 mg m^{-3} in Spring-Summer climatologies of satellite [Chl-a] (Figure 1).

The floats operated in the six zones defined above, covering HNLC as well as iron-fertilized areas, mainly in the Indian sector of the Southern Ocean. Given the wide range of physical and biogeochemical environments sampled, we believe that the float data set can be considered representative of Southern Ocean conditions, excepting areas with very deep (>500 m depth) winter mixing (Figure S7 in Supporting Information S1). We also note that the number of profiles was somewhat unevenly distributed between the different zones, with fewer profiles in the SIZ (Figures 5a–5f).

3. Results and Discussion

3.1. Regional and Seasonal Dynamics of Particles From the Productive Layer to 1,000 m Depth

3.1.1. Particle Dynamics in the Productive Layer

Particle concentration (b_{bp}) and phytoplankton biomass ([Chl-a]) show clear seasonal variations in the productive layer (Figures 5g–5l). The b_{bp} and [Chl-a] values started increasing in early spring and peaked during the produc-tive season, that is, spring and summer (Figures 5g–5l). This seasonal production of particles was initiated by the shallowing of MLD which increased the light exposure in the productive layer (Figure S7 in Supporting Infor-mation S1). These conditions promoted phytoplankton growth in the productive layer that had been replenished
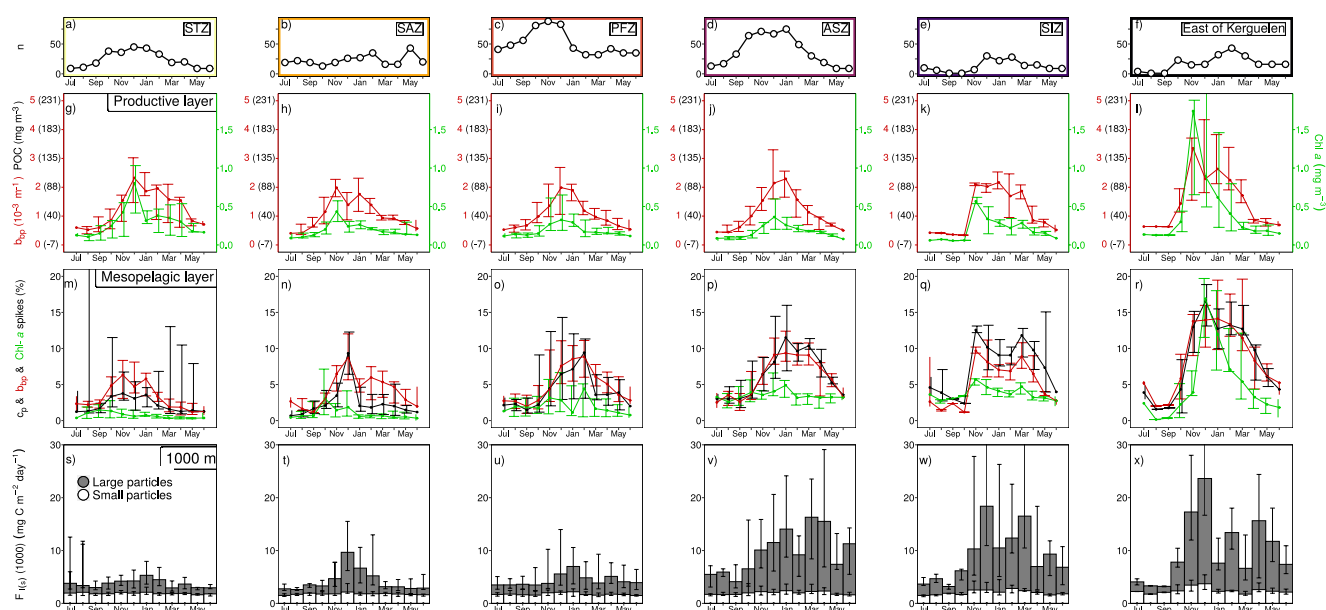
Figure 5. Regional and seasonal dynamics of particles from the productive layer to 1,000 m depth. For each zone, (a–f) number of profiles per month; monthly averages of (g–l) [Chl-a] (green) and b_{bp} (red) in the productive layer; (m–r) relative abundances of large particles (i.e., spikes) in the mesopelagic layer derived from b_{bp} (red), c_p (black), and [Chl-a] (green); (s–x) flux of large (gray bars) and small (white bars) particles at 1,000 m. The error bars represent the 15 and 85th quantiles. Figure S6 in Supporting Information S1 shows the number of float-year pairs for each zone (e.g., 1 pair = float 6902739–year2016).

with nutrients following deep convection in the preceding winter (Ardyna et al., 2017). The period following the maxima in bio-optical values corresponded to a rapid decline in [Chl-a] while b_{bp} remained elevated, leading to a higher bulk b_{bp}/[Chl-a] ratio of suspended particles (Figure S8 in Supporting Information S1). These particles in summer may correspond to less-chlorophyllous phytoplankton cells (Cetinić et al., 2015; Terrats et al., 2020) or non-algal particles such as detritus (Bellacicco et al., 2019).

Distinct seasonal cycles of b_{bp} and [Chl-a] were found in SIZ and East of Kerguelen, where the accumulation of particles soared in spring and led to the most abrupt rise in [Chl-a] and b_{bp} (Figures 5k and 5l). East of Kerguelen, the b_{bp} and [Chl-a] maxima were more than twice as high as typical maxima for HNLC zones. In the SIZ, b_{bp} and [Chl-a] maxima were similar to other HNLC zones, but b_{bp} remained at its maximum value over 4 months after the bloom apex. These distinctive characteristics suggest that additional processes were involved in the dynamics of particle accumulation in the SIZ and East of Kerguelen.

Sharp elevations of the sea floor characterize the area around the Kerguelen Islands, as evidenced by the presence of an oceanic plateau. This bathymetric feature is responsible for the supply of iron in the productive layer of the zone East of Kerguelen through the lateral advection of coastal waters or the entrainment of sedimentary material by deep mixing events (Bowie et al., 2015; d'Ovidio et al., 2015). This iron input markedly amplifies the division rate of phytoplankton, creating a decoupling between the phytoplankton growth and zooplankton grazing that may still be overwintering at depth (Carlotti et al., 2015; Laurenceau-Cornec et al., 2015). These conditions lead to the massive spring bloom observed East of Kerguelen (Blain et al., 2007). This zone thus represents a natural laboratory to study the impact of iron on the functioning of plankton communities and the resulting particle flux.

One main feature of the SIZ is the seasonal presence of sea-ice that plays a pivotal role in phytoplankton growth. Sea-ice melting releases iron that has been extracted from seawater during freezing or deposited from atmospheric dust (Lancelot et al., 2009; Person et al., 2021). Sea-ice melting also releases freshwater that causes a haline stratification of the water column and exposes the productive layer to intense sunlight (Figure S9 in Supporting Information S1). These conditions stimulate phytoplankton growth promptly while the grazing rate lags behind (Briggs et al., 2018; Person et al., 2021; Rohr et al., 2017), explaining the abrupt rise in b_{bp} and [Chl-a] in spring. Sea-ice melting continues in summer and sustains an intense production of particles associated with late phytoplankton blooms (Behera et al., 2020; Sabu et al., 2014), consistent with elevated b_{bp} observed until the end of summer.

3.1.2. Particle Dynamics in the Mesopelagic Layer

Some of the particles in the productive layer are exported in the form of large, fast-sinking particles. We addressed the dynamics of these large particles with observations of %Spikes, a proxy for the abundance of large particles in the mesopelagic layer (Briggs et al., 2011; Rembauville et al., 2017). For brevity, we discuss only the %Spikes from c_p measurements, denoted %Spikes $_{cp}$, as %Spikes estimated from b_{bp} and c_p measurements were similar ($r^2 = 0.81$).

Consistent with the seasonal production of particles, the abundance of large particles in the mesopelagic layer increased seasonally and peaked during the productive season (Figures 5m–5r). In HNLC zones, the peaks in %Spikes $_{cp}$ showed a latitudinal gradient in their magnitude, with a higher abundance of large particles South of the Polar Front (in zones ASZ and SIZ). The %Spikes $_{cp}$ South of the Polar Front averaged 9 ± 3% (mean ± standard deviation) during the productive season, versus 4 ± 2% North of the Polar Front (i.e., STZ, SAZ, PFZ) and decreased rapidly in Summer. East of Kerguelen, %Spikes $_{cp}$ remained elevated during the productive season as for South of the Polar Front, except that it reached higher levels amounting to 13 ± 5%. These observations suggest the establishment of a strong and persistent flux of large particles South of the Polar Front and East of Kerguelen, while the flux North of the Polar Front appears to be weaker and of shorter duration.

Using [Chl-a] measurements, we computed the %Spikes $_{[Chl-a]}$ as a proxy for the abundance of fresh phytoplankton aggregates in the mesopelagic layer. In HNLC zones, the %Spikes $_{[Chl-a]}$ during the productive season were characterized by low levels with 3 ± 1% South of the Polar Front, and 1 ± 1% North of the Polar Front. This is consistent with the identification of trap-collected particles in HNLC zones, which showed that most of the flux is carried by fecal material (Cavan et al., 2015, 2017; Ebersbach et al., 2011) and not phytoplankton aggregates. East of Kerguelen, the %Spikes $_{[Chl-a]}$ rose to 17% in spring then decreased rapidly to 7% in summer, indicating a transition in the nature of large particles from fresh algal aggregates in spring to non-chlorophyllous particles in summer such as fecal pellets and detrital aggregates, as reported by trap-based studies (Ebersbach & Trull, 2008; Laurenceau-Cornec et al., 2015; Rembauville, Blain, et al., 2015; Rembauville, Salter, et al., 2015).

3.1.3. Dynamics of Particle Fluxes at 1,000 m Depth

In HNLC zones, there is a clear latitudinal gradient in the seasonality and magnitude of the particle flux (Figure 5s-w). In the northernmost zone STZ, a very small fraction of particles originating from the phytoplankton bloom reached 1,000 m, as illustrated by the absence of strong seasonal variation and the low flux during the productive season (4.2 ± 0.8 mg C m^{-2} day^{-1}, which is the sum of large- and small-particle fluxes). Further South, in SAZ and PFZ zones, the particle flux varied seasonally with higher values during the productive season (5.5 ± 2.4 and 4.8 ± 1.3 mg C m^{-2} day^{-1}, respectively). South of the Polar Front, in ASZ and SIZ zones, the particle flux was highest with 11.3 ± 3.5 and 12.4 ± 4.5 mg C m^{-2} day^{-1}, respectively.

East of Kerguelen, the particle flux varied seasonally and peaked twice (Figure 5x). In spring, the flux sharply increased in November, similar to the particle concentration in the productive layer and the abundance of large particles in the mesopelagic layer. This simultaneous increase within the different depth layers suggests that the spring bloom led to a rapid and intense flux of large particles. At 1,000 m, this flux in spring represented a significant fraction of the total annual particle flux (40%). This result is similar to the results of Rembauville et al. (2015) on the Kerguelen Plateau based on sediment traps deployed at 300 m, which showed that the carbon flux in December and January constituted 40% of the annual flux. In late summer, the particle flux rose again and peaked in April (Figure 5x), following the depletion of particles in the productive and mesopelagic layers.

In zones South of the Polar Front and East of Kerguelen, the flux of large particles remained high (i.e., >7 mg C m^{-2} day^{-1}) until the end of Fall. This seasonal pattern was also reported with %Spikes $_{cp}$ and suggests that these regions were characterized by pulses of particles in late Summer and early Fall. This is confirmed with the identification of pulses in March in zones South of the Polar Front and East of Kerguelen, while none were observed after February in zones North of the Polar Front (Figure S10 in Supporting Information S1). These late pulses of large particles can be expected owing to phytoplankton blooms in late Summer in the SIZ (Behera et al., 2020; Sabu et al., 2014), to mixing events in fall that break down stratification and export particles retained in the surface (Kemp et al., 2000), or to the export of slower-sinking large particles originating from spring or summer phytoplankton blooms.
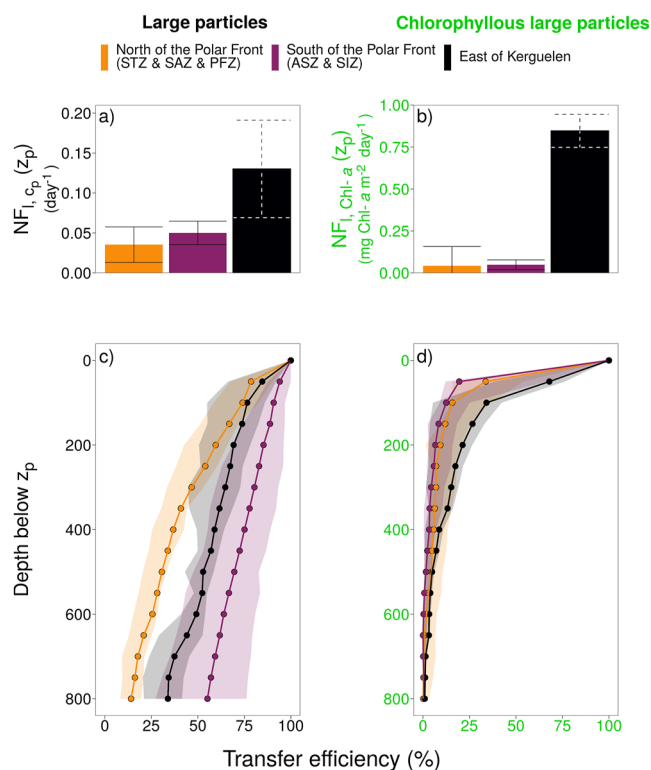
Figure 6. The downward transport of large-particles during the pulses. The net export flux and transfer efficiency of large-particles (a, c) and chlorophyllous particles (b, d) in the mesopelagic layer. Color indicates the zone. Median values are represented by bar height (a, b) or dots (c, d) with error bars (a, b) and ribbons (c, d) representing the 15 and 85th quantiles.

The flux of large particles at 1,000 m showed clear seasonal and latitudinal variations and represented 78% of the total particle flux. On the contrary, the flux of small particles was relatively constant and low throughout season and latitude, representing 22% of the total particle flux. Our observations confirm that large particles (i.e., fecal pellets and aggregates) are the main vector of carbon transport and sequestration in the Southern Ocean, consistent with ship-based and sediment trap observations (Cavan et al., 2015, 2017; Laurenceau-Cornec et al., 2015).

Our OST-based estimates of carbon flux at 1,000 m expressed above in units of mg C m^{-2} day^{-1} rely on the ATN-to-POC flux conversion (Equation 7), which has not been validated in the Southern Ocean. The lack of coincident, co-located observations of ATN flux with POC flux from sediment traps in the Southern Ocean precludes a direct comparison of approaches. Instead, we assessed general consistency by comparing annual fluxes from OST with annual fluxes from sediment traps reported in the literature. North (South) of the Polar Front we found 1.4 (3.3) g C m^{-2} year^{-1} for OST-based fluxes compared to 1.2 (2.6) g C m^{-2} year^{-1} from sediment traps compiled by Mouw et al. (2016b). In the SAZ, we found an annual POC flux of 1.6 g C m^{-2} year^{-1} from the OST compared to 1.2 g C m^{-2} year^{-1} from sediment traps (Wynn-Edwards et al., 2020). This comparison suggests good similarity in magnitude between the approaches.

3.2. Export and Transfer Efficiency of Large Particles in the Mesopelagic Layer

3.2.1. HNLC Waters

In HNLC zones, a clear southward increase in the large-particle flux at 1,000 m was observed while the particle concentration in the productive layer was similar between zones (Figure 5). This contrast was further evidenced by the southward increase in the ratio of the large-particle flux at 1,000 m over the b_{bp} values in the productive layer (Figure S11 in Supporting Information S1). These results indicate that variations in the flux at 1,000 m were not principally related to the particle concentrations at the surface and their seasonal variations in the productive layer, but rather to a higher export and/or transfer efficiency of large particles South of the Polar Front.

The high vertical and temporal resolution of the float profiles allowed the determination of the net export and transfer efficiency associated with the 17 pulses of large particles. For HNLC areas, we compared zones North and South of the Polar Front to determine if the export or transfer efficiency (or both) caused the southward increase in the flux at 1,000 m. The net export flux North and South of the Polar Front was similar, averaging 0.037 ± 0.023 days^{-1} and 0.045 ± 0.013 days^{-1}, respectively. The transfer efficiency was, however, three times higher South of the Polar Front, with 57% of the exported flux reaching the deepest layer of the mesopelagic layer (i.e., zp+800–1,000 m), compared to 17% North of the Polar Front (Figure 6). This observation indicates that a higher proportion of large particles escaped degradation in the mesopelagic layer South of the Polar Front. These observations are in line with thorium measurements of POC flux and transfer efficiency by Puigcorbé et al. (2017). The authors reported similar export flux North and South of the Polar Front, while transfer efficiencies at 400 m were threefold higher in waters South of the Polar Front (Table 3 in Puigcorbé et al. (2017)). The Polar Front thus clearly delimits zones with distinct mesopelagic transfer efficiency and deep POC flux.

We then investigated the causes of this contrast in transfer efficiency. Differences in transfer efficiency result, to first order, from the balance between the degradation rate and sinking speed of particles in the mesopelagic layer. Some degradation processes are temperature-dependent and their magnitude can be predicted from temperature measurements (Kheireddine et al., 2020; Marsay et al., 2015). For the large-particle pulses observed here, temperature in the mesopelagic was lower by 3 ± 1°C on average in zones South of the Polar Front (Figure S12 in Supporting Information S1), which corresponds to a calculated increase of 41% in the transfer efficiency (see

Text S3 in Supporting Information S1 for further details on the calculation). This is insufficient to explain the three-fold increase in transfer efficiency South of the Polar Front, and suggests that other processes come into play.

Fragmentation of large into small particles is another degradation process which was found to be responsible for about half of the attenuation of large-particle flux (Briggs et al., 2020). The study of Briggs et al. (2020) explored 34 pulses to quantify the transfer of mass from large to small particles during their sinking in the mesopelagic layer. In the Southern Ocean, they noted high variability in fragmentation rate that contributed between 30% and 72% to flux attenuation. Using their results (Table S2 in Briggs et al. (2020)), we assessed differences in the fragmentation rates between zones North and South of the Polar Front. These data indicated that fragmentation was responsible for 36% of the flux attenuation North of the Polar Front (Table S4 in Supporting Information S1). South of the Polar Front, fragmentation was relatively more important and contributed 55% to flux attenuation. This result goes counter our observations and suggests that the higher transfer efficiency South of the Polar Front was not the result of a lower fragmentation of large particles.

A faster sinking speed shortens the residence time of particles in the mesopelagic layer where they are exposed to degradation processes, thus increasing their transfer efficiency. According to Stokes Law, the sinking speed of spherical particles scales as the square of their size times their density in excess of the density of seawater. Laboratory-based studies indicate that the typical sinking speed of small particles varies between 0.1 and 10 m day^{-1} for individual phytoplankton cells (Huisman & Sommeijer, 2002; Waite et al., 1997), whereas it exceeds 100 m day^{-1} for large particles such as aggregates and fecal pellets (Iversen & Ploug, 2013). Although sinking speed also depends on other factors, such as the particle shape, fractal dimension, porosity, and composition (Williams & Giering, 2022), particle size is still widely used as the primary indicator of in situ particle sinking speed (Cael et al., 2021; Guidi et al., 2008; Iversen et al., 2010; Omand et al., 2020). Here, we derived an optical proxy for the average diameter of large particles in the mesopelagic by averaging the heights of mesopelagic c_p spikes (Briggs et al., 2013; McKenzie et al., 2020). South of the Polar Front, spike heights averaged 0.0040 ± 0.0005 m^{-1}, as compared to 0.0018 ± 0.0006 m^{-1} North of the Polar Front (Figure S13 in Supporting Information S1). These results show that aggregates and fecal pellets were significantly larger in the mesopelagic layer South of the Polar Front, which condition their higher sinking speed and transfer efficiency.

3.2.2. Iron-Fertilized Area

East of Kerguelen, most of large-particle pulses were sampled in November (Figure S10 in Supporting Information S1) and therefore our results in Figure 6 mainly represent spring conditions. The net export flux equaled 0.135 days^{-1} and was three times higher than in HNLC waters (0.037 and 0.045 days^{-1} for North and South of the Polar Front, respectively). This is qualitatively consistent with ship-based observations of a two-fold higher export flux of POC in the iron-fertilized area in spring as compared to export flux in HNLC waters (Planchon et al., 2015). The transfer efficiency of large-particle flux East of Kerguelen was 41%, intermediate between transfer efficiencies in zones North and South of the Polar Front (17% and 57%, respectively). However, the average diameter of large particles, the water temperature, and the attenuation due to fragmentation were similar to zones South of the Polar Front (Figures S11, S12, and Table S4 in Supporting Information S1, respectively), suggesting other influences on transfer efficiency such as the lability and composition of the sinking particles.

The hypothesis that transfer efficiency decreases with the lability of particles has been advanced in multiple studies (e.g., Henson et al., 2012; Marsay et al., 2015; Rosengard et al., 2015; Stukel et al., 2018). Fresh particles that have been slightly recycled by heterotrophic organisms contain an important fraction of labile material that is prone to rapid remineralization in the mesopelagic layer. East of Kerguelen, large particles were rich in Chl-*a* as illustrated by the high export of chlorophyllous aggregates (0.48 mg Chl-*a* m^{-2} day^{-1}) (Figure 6b) and transfer efficiency superior to 10% in the first 350 m of the mesopelagic layer (Figure 6d). This indicates that some aggregates remained chlorophyllous while sinking through the upper mesopelagic layer. These results, in line with in situ observations of mesopelagic phyto-aggregates in this zone (Jouandet et al., 2014; Rembauville, Blain, et al., 2015; Rembauville, Salter, et al., 2015), reflect the freshness of the exported large particles. Conversely, observations in HNLC waters indicated that large particles were essentially non-chlorophyllous as evidenced by the low export and rapid attenuation of chlorophyllous aggregates in the mesopelagic layer (Figures 6b and 6d), suggesting the predominance of recycled material such as fecal pellets and detrital aggregates in the mesopelagic layer of HNLC zones, as reported by ship-based measurements (Cavan et al., 2015, 2017). This distinction in the freshness of particles was also observed during the pulses of small particles (Figure S14 in Supporting Information S1), with the presence of chlorophyllous
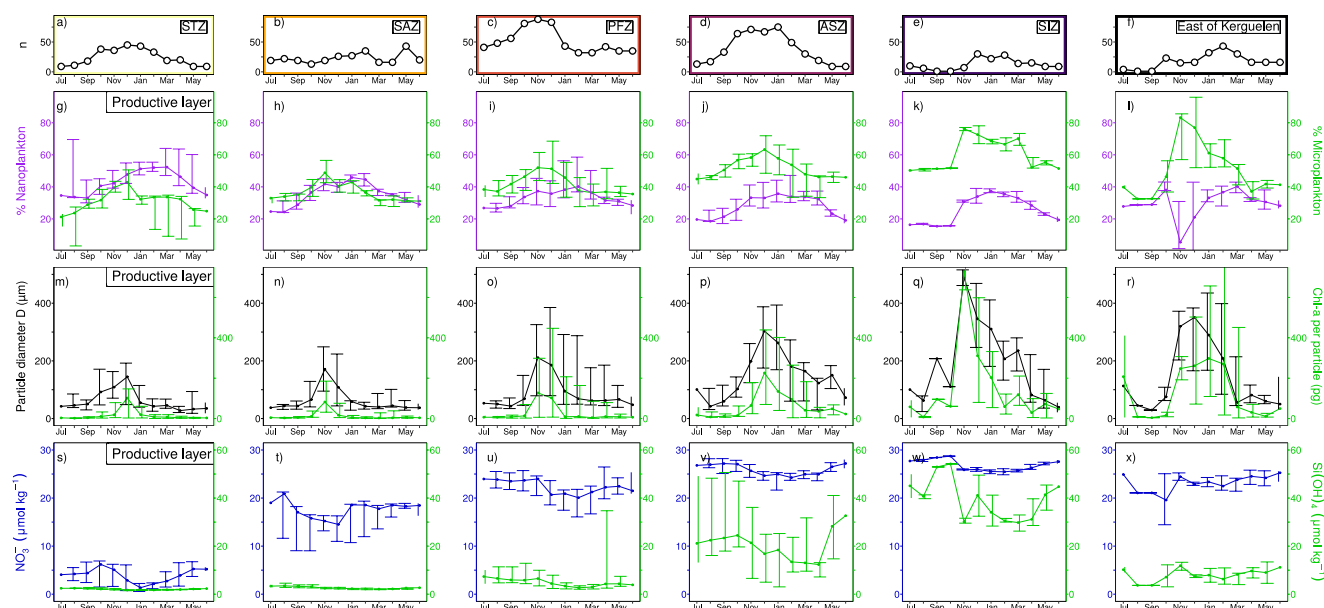
Figure 7. Regional and seasonal variations of metrics characteristic of the size of phytoplankton and particles in the productive layer. For each zone, (a–f) the number of profiles per month; monthly climatologies in the productive layer of (g–l) the proportions of Nano- (purple) and Micro-plankton (green); (m–r) the diameter (black) and [Chl-a]-content (green) of large-particles; (s–x) the concentrations in [NO_3^-] (blue) and [$Si(OH)_4$] (green) derived from CANYON-B (Bittig, Körtzinger, et al., 2018; Bittig, Steinhoff, et al., 2018; Sauzède et al., 2017). The error bars represent the 15 and 85th quantiles. Figure S6 in Supporting Information S1 shows the number of float-year pairs for each zone (e.g., 1 pair = float 6902739–year2016).

material East of Kerguelen which was likely originating from the fragmentation of fragile phyto-aggregates. These results on the freshness of particles suggest that the lower transfer efficiency East of Kerguelen compared to South of the Polar Front may result from the important fraction of labile material that constitutes the large-particle flux.

Another factor is the mineral content of particles. Minerals, such as Si, enhance the transfer efficiency by increasing the density and sinking rate of particles (Armstrong et al., 2002). Si-ballasted particles tend to sink faster than non-ballasted particles and are more efficiently transferred to depth (Tréguer et al., 2018). For example, copepod fecal pellets produced from a diatom diet sink faster and withstand microbial breakdown better (Ploug et al., 2008). Silicification of diatom cells directly impacts the cell density that in turn modifies the sinking rate by a factor of two to seven (Baines et al., 2010; Tréguer et al., 2018). Silicification of diatom cells has been shown to increase with iron limitation (Takeda, 1998), suggesting that the cells are heavily silicified in HNLC waters compared to iron-fertilized areas. This has been confirmed in the Southern Ocean where the particulate biomass is composed of a greater proportion of heavily silicified particles in HNLC waters, as compared to iron fertilized sites East of Kerguelen (Lafond et al., 2020; Rembauville et al., 2018) and North of Crozet Islands (Salter et al., 2012). Thus, the heavy silicification of diatom cells in the HNLC waters South of the Polar Front might also contribute to the higher transfer efficiency compared to East of Kerguelen.

3.3. Predicting Large-Particle Flux From Surface Variables

3.3.1. Surface Drivers of the Gravitational Pump

Float data provided insights into surface drivers of the gravitational pump by capturing the nature of particles in the productive layer (Briggs et al., 2013) and the size-structure of the phytoplankton community (Rembauville et al., 2017). In the HNLC waters South of the Polar Front, the micro-phytoplankton comprised $58 \pm 5\%$ of the phytoplankton community during the productive season (Figures 7j and 7k), likely dominated by diatoms, as shown in ship-based studies (Deppeler & Davidson, 2017; Trull et al., 2001; Viljoen et al., 2018) and supported by observations of heavy $SiOH_4$ drawdown (Figures 7v-w and Figure S15 in Supporting Information S1). The dominance of diatoms was associated with the production of the largest particles (Figures 7p and 7q) that potentially sink fast in the mesopelagic layer. This formation of large particles can also be linked to grazing by large zooplankton species, such as salps, krill, and large copepods that feed on diatom populations South of the Polar

Front and produce large fecal-pellets sinking at several hundreds of meters per day (Cavan et al., 2019; Pauli et al., 2021; Puigcorbé et al., 2017).

North of the Polar Front, the proportion of nano-phytoplankton increased equatorward and becomes predominant year-round in the STZ (Figures 7g–7i). The phytoplankton community comprises greater contributions of smaller phytoplankton groups belonging to nano-phytoplankton including coccolithophores, other prymnesiophytes and flagellates (Deppeler & Davidson, 2017; Trull et al., 2001; Viljoen et al., 2018), which result in the formation of smaller particles in the productive layer (Figures 7m–7o). These results thus indicate that the Polar Front marks a substantial change in the composition of the phytoplankton community and in the nature of particles produced at the surface.

East of Kerguelen, the micro-phytoplankton outcompete other phytoplankton size classes during the productive season as illustrated by %Micro values of $57 \pm 5\%$ (Figure 7l). This is consistent with ship-based studies identifying diatoms as the main bloom-formers in response to natural iron fertilization in this area (Armand et al., 2008; Blain et al., 2021; Lasbleiz et al., 2016). Compared to SIZ and SAZ waters also dominated by diatoms, the bloom East of Kerguelen was associated with a lower decrease in $SiOH_4$ (Figure 7x; Figure S14 in Supporting Information S1). This was expected as diatoms were expected to be only slightly silicified in these iron-fertilized areas compared to HNLC waters (Lafond et al., 2020; Rembauville et al., 2018).

These results indicate that zones with a high magnitude and transfer efficiency of large-particle flux were characterized by a clear predominance of micro-phytoplankton, such as South of the Polar Front. This agrees with regional studies suggesting that the more micro-phytoplankton are present in the productive layer, the higher the probability for the formation of large and fast-sinking particles (Mouw et al., 2016a; Wiedmann et al., 2020). Our study thus confirms a strong link between the gravitational pump and the size parameters of the plankton ecosystem structure in the Southern Ocean, which can be leveraged to model the flux at 1,000 m from surface predictors.

3.3.2. Models for Predicting Large-Particle Flux at 1,000 m

We set up two models to estimate the large-particle flux at 1,000 m using size parameters and concentration of particles in the surface layer. The first model is based on the product of b_{bp} (m^{-1}) and the square of particle diameter (μm), D, both averaged in the productive layer:

$$F_l (1000) \left(mg\,C\,m^{-2}\,day^{-1} \right) = a_1 \times b_{bp} \times D^2 \qquad (13)$$

where a_1 has units of mg C 10^{-12} m^{-3} day^{-1}. Equation 13 can be seen as a model to estimate the flux at 1,000 m based on a proxy for [POC] in the productive layer (i.e., b_{bp}) multiplied by a proxy for transfer efficiency in the mesopelagic layer (i.e., D^2). This is because transfer efficiency is, to first order, the balance between the degradation rate and sinking speed of a particle, which, according to Stokes' law, scales as the square of particle diameter (D^2). Even though marine particles are rarely spherical, we explore here the utility of D^2 as a proxy for the transfer efficiency of the flux. Similarly, the second model uses the product of b_{bp} (m^{-1}) and the square of %Micro (%) in the top 15 m of the productive layer, so that it can be directly applied to satellite observations of the ocean surface and might provide ways of upscaling large-particle flux at 1,000 m:

$$F_l (1000) \left(mg\,C\,m^{-2}\,day^{-1} \right) = a_2 \times b_{bp} \times \%Micro^2 \qquad (14)$$

where a_2 has units of mg C m^{-1} day^{-1}. To determine the coefficients a_1 and a_2 of Equations 13 and 14, respectively, we leveraged the quasi-Lagrangian sampling of pulses to associate surface b_{bp}, %Micro, and D to the resulting flux of large particles at 1,000 m (see the values on Table S3 in Supporting Information S1). We averaged the surface variables over the period of intense particle production that we graphically delineated by the seasonal increasing phase in b_{bp} and [Chl-a] in the productive layer (Figure S16a in Supporting Information S1). At 1,000 m, we averaged the large-particle flux over a time-window corresponding to the pulse in the mesopelagic layer extended by several days until the flux at 1,000 m returned to low levels (6 ± 10 days on average, Figure S16c in Supporting Information S1). This was required to consider the time gap between the end of the pulse in the mesopelagic layer and the pulsed signal at 1,000 m. The sensitivity of the coefficients a_1 and a_2 to displacement of time windows are shown in Figure S17 in Supporting Information S1.

Using these match-ups, we determined a_1 and a_2 as the slope of the linear regression forced through the origin, yielding $a_1 = 0.077 \pm 0.079$ mg C 10^{-12} m^{-3} day^{-1} and $a_2 = 1.48 \pm 0.59$ mg C m^{-1} day^{-1} (Figure 8). The
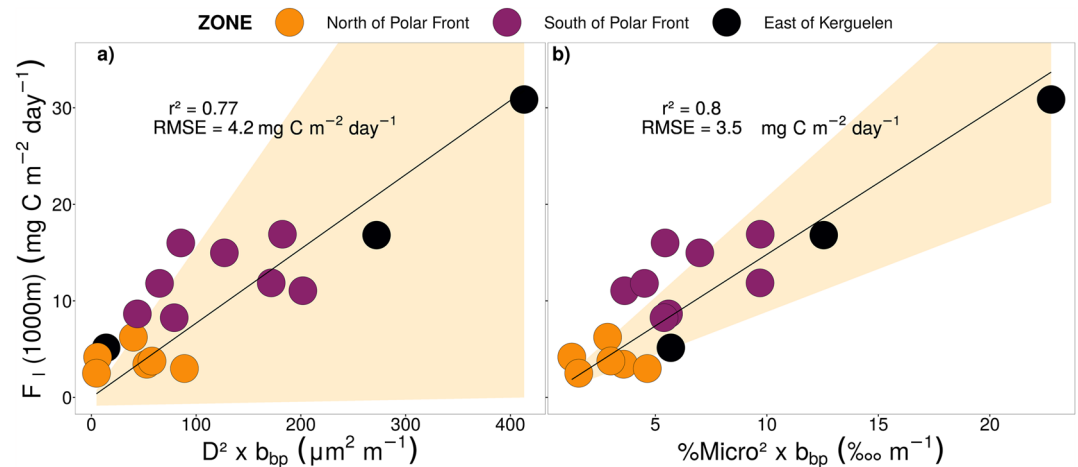
Figure 8. Co-variation during large-particle pulses between the large-particle flux at 1,000 m and the product of (a) squared particle diameter and b_{bp} in the productive layer, (b) squared %Micro and b_{bp} in the first 15 m. The black line is the least-square regression line. The orange area illustrates the uncertainty in the coefficients (a) a_1 and (b) a_2. The point color refers to the zones.

uncertainty of a_1 and a_2 corresponds to the standard deviation of the slopes that we obtained after repeating the fit 10000 times with the introduction of errors in %Micro (17%, Rembauville et al. (2017)), D (150%, Briggs et al. (2013)), and $F_l(1,000\,\text{m})$ (19.4 mg C m^{-2} day^{-1}, Estapa et al. (2023)). These regressions captured most of the variability in the large-particle flux at 1,000 m, with a coefficient of determination $r^2 = 0.77$ and 0.80 and a Root-Mean-Square-Error (RMSE) of 4.2 and 3.5 mg C m^{-2} day^{-1} for Equations 13 and 14, respectively. Furthermore, the models were determined with pulse data sampled from all major Southern Ocean ecosystems, including HNLC waters on both sides of the Polar Front and naturally iron-fertilized areas, suggesting that Equations 13 and 14 may be applicable in other sectors of the Southern Ocean.

It is worth mentioning that the correlation between $b_{bp} \times D^2$ and $F_l(1,000\,\text{m})$ was also observed with $b_{bp} \times D$ ($r^2 = 0.75$). This suggests that other particle properties affecting the transfer efficiency are size-dependent. The density of particles, for example, has been shown to scale as the inverse of D in a wide range of marine environments (Neukermans et al., 2012), and/or particle degradation rates may also be size-dependent.

We tested the models on the monthly climatologies of F_l (1,000 m), b_{bp}, D, and %Micro depicted in Figures 5 and 7. Equations 13 and 14 were applied to the monthly climatologies of b_{bp}, D, and *%Micro* values (displayed on Figures 5g–5l and 7g–7r), and the flux estimates were compared to the monthly climatology of flux measurements (displayed on Figures 5s–5x). These comparisons showed that the two models retrieved the large-particle flux at 1,000 m with reasonable accuracy, when predictors were averaged over the productive season (RMSE = 2.6 and 1.9 mg C m^{-2} day^{-1} for Equations 13 and 14, respectively, Figures S18 and S19 in Supporting Information S1). Averaging the predictors over the productive season permitted to account for the time lag between the flux estimated with surface predictors and the flux measured at 1,000 m due to the sinking time of particles in the mesopelagic layer. This analysis thus confirmed that Equations 13 and 14 can be used to predict the mean flux of large particles during the productive season (i.e., Spring-Summer, or October to March).

Next, we upscaled flux estimates at the scale of the Southern Ocean by including surface measurements from floats (Section 3.3.3) and satellites (Section 3.3.4). We averaged the surface measurements over the productive Spring-Summer season (October-March) and applied Equations 13 and 14 to estimate the mean flux of large particles over the productive season. The resulting flux was then multiplied by 183 days to derive the total flux of large particles over the productive season, hereafter referred to as "Spring-Summer flux," F_{lSS} (1000 m):

$$F_{l\,SS}(1000)\,(\text{mgC m}^{-2}) = a_1 \times \text{seasonal } b_{bp} \times \text{seasonal } D^2 \times 183\,\text{days} \tag{15}$$

$$F_{l\,SS}(1000)\,(\text{mgC m}^{-2}) = a_2 \times \text{seasonal } b_{bp} \times \text{seasonal } \%\text{Micro}^2 \times 183\,\text{days} \tag{16}$$
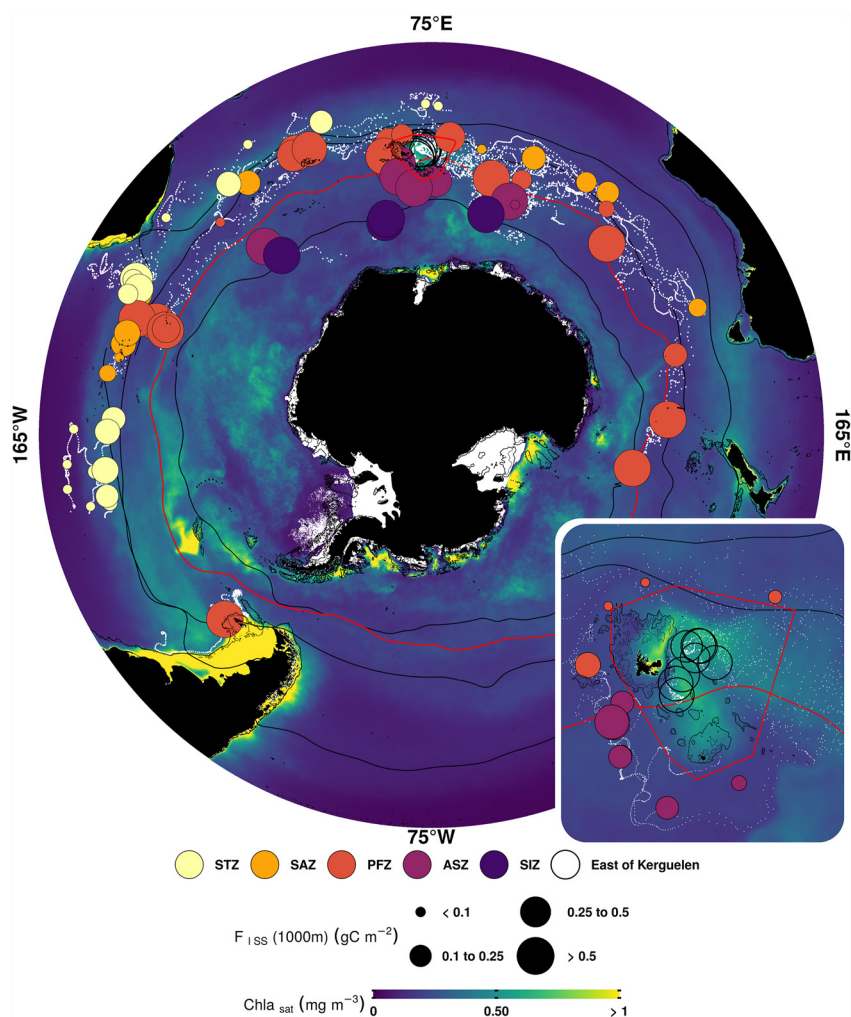
Figure 9. Spatial variability in the Spring-Summer flux of large particles at 1,000 m derived from float data (Equation 15). The dots show the mean position of the float during the productive season. The dot size indicates the intensity of the estimated flux, and their color refers to the various zones. The red line represents the position of the Polar Front, while the black lines represent the positions of other fronts. The boundaries of the zone "East of Kerguelen" are drawn in red and detailed in the bottom right insert. The background map is the Spring-Summer climatology (2015–2019) of satellite [Chl-a]. The thin black lines are the 200 and 400 m bathymetry contours.

with the prefix "seasonal" indicating that b_{bp}, D, and %Micro were averaged over the productive Spring-Summer season. In the following sections, we averaged Spring-Summer flux over several zones and expressed the results as the mean $\pm$ standard deviation of F_{ISS} (1,000).

3.3.3. Application to Other Floats in the Southern Ocean

To upscale our observations of Spring-Summer flux, we first applied the model based on Equations 15–26 floats operating mainly in the Indian and Atlantic sectors of the Southern Ocean using particle diameter estimates from b_{bp} measurements in the productive layer. This permitted to obtain a broader view of the spatial variability in the Spring-Summer flux as shown in Figure 9. As expected, the latitudinal patterns obtained from upscaling were the same as observed with the smaller data set: the Spring-Summer flux was higher South of the Polar Front compared to North (0.63 $\pm$ 0.51 vs. 0.3 $\pm$ 0.36 g C m^{-2} respectively) and fluxes East of Kerguelen were the highest, averaging 1.70 $\pm$ 0.66 g C m^{-2}. Moreover, upscaling also permitted the discovery of regions with unexpectedly intense Spring-Summer flux North of the Polar Front, such as the Shona Ridge System (43–53°S, 1 to 10°E) with a Spring-Summer flux of 0.47 $\pm$ 0.14 g C m^{-2}. This area comprises seamounts shallower than 100 m that create a mass effect in contact with the Antarctic Circumpolar Current, fertilizing downstream waters
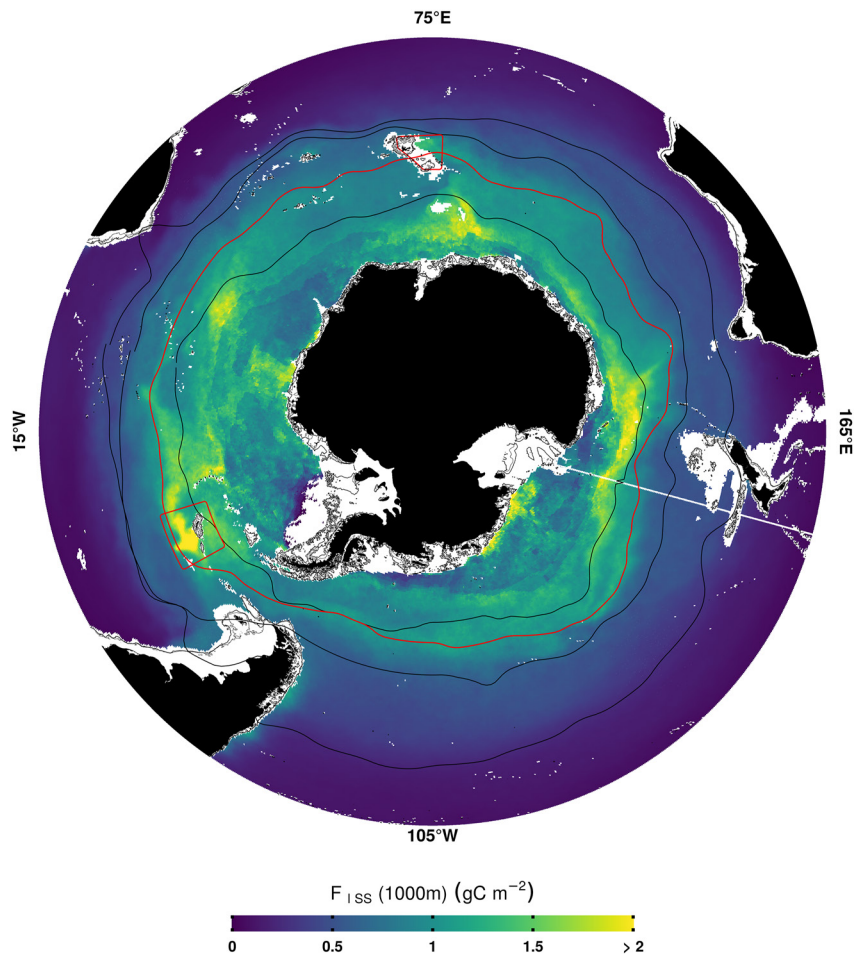
Figure 10. Spatial distribution in the Spring-Summer flux of large-particle at 1,000 m derived from satellite data. The map is the 2002–2021 climatology of the large-particle flux at 1,000 m during the productive season (i.e., October-March) obtained from Equations 16 and 17. The red rectangles represent major iron-fertilized areas of the Southern Ocean (i.e., East of Kerguelen and South Georgia). The red line represents the position of the Polar Front while the black lines are the positions of other fronts (from north to south: STF, SAF, PF (in red), and the northern limit of SIZ). The thin black lines are the 200 and 400 m bathymetry contours.

with sedimentary iron, and fostering intense phytoplankton blooms (Sergi et al., 2020). Other iron-fertilized areas sampled by floats also exhibited an intense Spring-Summer flux, such as the area North of Crozet islands (43–47°S, 49 to 57°E) with a Spring-Summer flux of 0.45 ± 0.02 g C m^{-2}.

3.3.4. Application to Satellite Data

We also estimated the Spring-Summer flux for the whole Southern Ocean by applying Equation 16 to satellite data from 2002 to 2021. For %Micro we used the satellite product of Xi et al. (2020), which compared well to %Micro from float data (Figure S20 in Supporting Information S1; $r^2 = 0.5$; RMSE = 14%), while for b_{bp} we used the 3D fields of b_{bp} (700) over the first 15 m estimated by the SOCA-BBP method, which has been trained, tested, and validated with b_{bp} float data (product accessible here https://doi.org/10.48670/moi-00046 and based on Sauzède et al. (2016)). We averaged the parameters %Micro and b_{bp} over the productive season, that is, spring and summer, and used Equation 16 to obtain the Spring-Summer flux for each year.

When calculated in this manner, the Spring-Summer flux corresponds to the average flux for the ice-free period of the productive season. This is because the products of %Micro and b_{bp} only cover the ice-free period. We adjusted the Spring-Summer flux to represent the entire productive season using the findings that the POC flux is negligible when the sea-ice concentration exceeds 85%, as revealed by concurrent measurements of POC flux and sea-ice (Garrity et al., 2005; Kim et al., 2015). To achieve this, we multiplied the Spring-Summer flux obtained

from Equation 16 by the proportion of the productive season with a sea-ice concentration below 85% (monthly maps of sea-ice concentration were obtained from https://psl.noaa.gov at the resolution of 0.25°):

$$F_{1SS}(1000)\left(\mathrm{mgC\,m^{-2}}\right) = F_{1SS}(1000)\,\text{from Eq.16} \times \frac{nb\ \text{month with sea ice cover} < 85\%}{6} \quad (17)$$

Finally, we averaged the Spring-Summer flux maps to obtain a 2002–2021 climatology of Spring-Summer flux in the Southern Ocean (Figure 10).

Spatial patterns in the Spring-Summer flux climatology of the Southern Ocean obtained from satellite data were consistent with spatial patterns obtained from floats. The Spring-Summer flux was more intense South of the Polar Front compared to North with respective average fluxes of 1.08 ± 0.27 and 0.41 ± 0.25 g C m^{-2}. The satellite-derived flux was highest in iron-fertilized areas, reaching values of 1.15 ± 0.17 g C m^{-2} East of Kerguelen and 1.51 ± 0.36 g C m^{-2} South Georgia islands, where lateral advection extracts sedimentary iron from the shore and fertilizes the downstream waters (Borrione et al., 2014; Nielsdóttir et al., 2012). The average Spring-Summer flux was 0.83 ± 0.36 g C m^{-2} (spatial average for waters South of 40°S), whereas the basin-integrated Spring-Summer flux was 0.054 Pg C with an uncertainty of 0.021 Pg C (based on uncertainty in a_2).

By comparing this new estimate of basin-integrated flux at 1,000 m with estimates of organic carbon export at the surface, we can gain a deeper understanding of the Southern Ocean gravitational pump. Previous observational and modeling estimates for Southern Ocean annual export or Annual Net Community Production (ANCP, i.e., the amount of carbon fixed during photosynthesis i.e., not remineralized in the surface layer, which should balance with annual export at steady state and over long space scales >1,000) range between 1.99 Pg C year^{-1} to 3.89 Pg C year^{-1} (MacCready & Quay, 2001; Su et al., 2022). Based on our basin-wide Spring-Summer flux at 1,000 m of 0.054 ± 0.021 Pg C, this suggests that 1.4%–2.7% of the annually exported carbon is transported to 1,000 m in Spring-Summer by the gravitational pump in the form of large particles. This is close to the observations of 2%–3% by Wynn-Edwards et al. (2020), who compared the ANCP to the annual POC flux of small and large particles in the SAZ. This suggest that the gravitational pump, through the transport of large particles in Spring-Summer, may be responsible for most of the transport of POC to 1,000 m in the Southern Ocean.

4. Conclusions

In this study we performed an in-depth examination of the gravitational pump of the Southern Ocean based on observations from BioGeoChemical-Argo floats and satellites. Novel methodologies were developed to observe and characterize POC flux in the mesopelagic zone. Our results reveal a clear seasonality and southward increase in POC flux at 1,000 m owing to an increase in the transfer efficiency of the mesopelagic POC flux, which was in turn linked to the size structure of the surface planktonic ecosystem. In the southernmost HNLC zones, the magnitude of the large-particle flux at 1,000 m was similar to the zone East of Kerguelen where iron-fertilization increases production and export of particles.

By combining observations of particles in the productive surface layer with particle flux observations in the mesopelagic zone, we demonstrated a linkage between the flux of large particles at 1,000 m and the characteristics of surface ecosystems. Variability in deep flux was driven by changes in the composition of the phytoplanktonic community and the size of particles, with intense flux associated with the predominance of micro-phytoplankton and large particles. This linkage allowed us to upscale our particle flux survey across the entire Southern Ocean based on observations of surface variables, either obtained from other BGC-Argo floats or satellites. The upscaled observations showed a basin-wide latitudinal increase in large-particle flux at 1,000 m, where the Polar Front marked a divide in magnitude and functioning of the gravitational pump. These results also identified areas of natural iron fertilization as hotspots of carbon sequestration, and suggested the predominance of the gravitational pump in carbon sequestration below 1,000 m. Lastly, we obtained a new estimate of basin-wide Spring-Summer flux at 1,000 m of sinking particles over the Southern Ocean of 0.054 ± 0.021 Pg C.

This work opens perspectives for a better understanding of the gravitational pump using the growing array of BGC-Argo floats equipped with a transmissometer that operates as an OST (Claustre et al., 2021). By estimating the POC flux from transmissometers or surface variables, BGC-Argo floats can provide basin-wide characterizations of the gravitational pump at unique spatio-temporal resolutions. Pending future deployments of floats

with an OST and other carbon flux sensors, such as the Underwater Vision Profiler (Picheral et al., 2022) and particulate inorganic carbon sensors (Bishop et al., 2022; Neukermans et al., 2023), the global array of floats has the potential to fill important knowledge gaps in global ocean carbon sequestration and its linkage with surface ocean ecosystems.

Conflict of Interest

The authors declare no conflicts of interest relevant to this study.

Data Availability Statement

All BGC-Argo data are available at https://doi.org/10.17882/42182 or ftp://ftp.ifremer.fr/ifremer/argo/dac/ (Argo, 2023). These data were collected and made freely available by the International Argo Program and the national programs that contribute to it (http://www.argo.ucsd.edu, http://argo.jcommops.org). The data supporting the conclusions of this study are freely available at https://doi.org/10.17882/94676 (Terrats et al., 2023) and were analyzed using R software (R Core Team, 2022; RStudio Team, 2022).

References

Antoine, D., & Morel, A. (1996). Oceanic primary production: 1. Adaptation of a spectral light-photosynthesis model in view of application to satellite chlorophyll observations. *Global Biogeochemical Cycles*, *10*(1), 43–55. https://doi.org/10.1029/95GB02831

Ardyna, M., Claustre, H., Sallée, J.-B., D'Ovidio, F., Gentili, B., van Dijken, G., et al. (2017). Delineating environmental control of phytoplankton biomass and phenology in the Southern Ocean. *Geophysical Research Letters*, *44*(10), 5016–5024. https://doi.org/10.1002/2016GL072428

Argo (2023). Argo float data and metadata from global data assembly Centre (Argo GDAC). SEANOE, Ed. https://doi.org/10.17882/42182

Armand, L. K., Cornet-Barthaux, V., Mosseri, J., & Quéguiner, B. (2008). Late summer diatom biomass and community structure on and around the naturally iron-fertilised Kerguelen Plateau in the Southern Ocean. *Deep Sea Research Part II: Topical Studies in Oceanography*, *55*(5), 653–676. https://doi.org/10.1016/j.dsr2.2007.12.031

Armstrong, R. A., Lee, C., Hedges, J. I., Honjo, S., & Wakeham, S. G. (2002). A new, mechanistic model for organic carbon fluxes in the ocean based on the quantitative association of POC with ballast minerals. *Deep-Sea Research Part II Topical Studies in Oceanography*, *49*(1–3), 219–236. https://doi.org/10.1016/S0967-0645(01)00101-1

Arteaga, L., Haëntjens, N., Boss, E., Johnson, K. S., & Sarmiento, J. L. (2018). Assessment of export efficiency equations in the southern ocean applied to satellite-based net primary production. *Journal of Geophysical Research: Oceans*, *123*(4), 2945–2964. https://doi.org/10.1002/2018JC013787

Baines, S. B., Twining, B. S., Brzezinski, M. A., Nelson, D. M., & Fisher, N. S. (2010). Causes and biogeochemical implications of regional differences in silicification of marine diatoms. *Global Biogeochemical Cycles*, *24*(4). https://doi.org/10.1029/2010GB003856

Behera, N., Swain, D., & Sil, S. (2020). Effect of Antarctic sea ice on chlorophyll concentration in the Southern Ocean. *Deep Sea Research Part II: Topical Studies in Oceanography*, *178*, 104853. https://doi.org/10.1016/j.dsr2.2020.104853

Bellacicco, M., Cornec, M., Organelli, E., Brewin, R. J. W., Neukermans, G., Volpe, G., et al. (2019). Global variability of optical backscattering by non-algal particles from a biogeochemical-Argo data set. *Geophysical Research Letters*, *46*(16), 9767–9776. https://doi.org/10.1029/2019gl084078

Bishop, J. K. B., Amaral, V. J., Lam, P. J., Wood, T. J., Lee, J.-M., Laubach, A., et al. (2022). Transmitted cross-polarized light detection of particulate inorganic carbon concentrations and fluxes in the ocean water column: Ships to ARGO floats. *Frontiers in Remote Sensing*, *3*. https://doi.org/10.3389/frsen.2022.837938

Bishop, J. K. B., & Wood, T. J. (2009). Year-round observations of carbon biomass and flux variability in the Southern Ocean. *Global Biogeochemical Cycles*, *23*(2), 1–12. https://doi.org/10.1029/2008GB003206

Bittig, H. C., & Körtzinger, A. (2015). Tackling oxygen optode drift: Near-surface and in-air oxygen optode measurements on a float provide an accurate in situ reference. *Journal of Atmospheric and Oceanic Technology*, *32*(8), 1536–1543. https://doi.org/10.1175/JTECH-D-14-00162.1

Bittig, H. C., Körtzinger, A., Neill, C., van Ooijen, E., Plant, J. N., Hahn, J., et al. (2018). Oxygen optode sensors: Principle, characterization, calibration, and application in the ocean. *Frontiers in Marine Science*, *4*. https://doi.org/10.3389/fmars.2017.00429

Bittig, H. C., Maurer, T. L., Plant, J. N., Wong, A. P., Schmechtig, C., Claustre, H., et al. (2019). A BGC-Argo guide: Planning, deployment, data handling and usage. In *Frontiers in marine science* (Vol. 6). Frontiers Media S.A. https://doi.org/10.3389/fmars.2019.00502

Bittig, H. C., Steinhoff, T., Claustre, H., Fiedler, B., Williams, N. L., Sauzède, R., et al. (2018). An alternative to static climatologies: Robust estimation of open ocean CO_2 variables and nutrient concentrations from T, S, and O_2 data using Bayesian neural networks. *Frontiers in Marine Science*, *5*. https://doi.org/10.3389/fmars.2018.00328

Blain, S., Quéguiner, B., Armand, L., Belviso, S., Bombled, B., Bopp, L., et al. (2007). Effect of natural iron fertilization on carbon sequestration in the Southern Ocean. *Nature*, *446*(7139), 1070–1074. https://doi.org/10.1038/nature05700

Blain, S., Rembauville, M., Crispi, O., & Obernosterer, I. (2021). Synchronized autonomous sampling reveals coupled pulses of biomass and export of morphologically different diatoms in the Southern Ocean. *Limnology & Oceanography*, *66*(3), 753–764. https://doi.org/10.1002/lno.11638

Borrione, I., Aumont, O., Nielsdóttir, M. C., & Schlitzer, R. (2014). Sedimentary and atmospheric sources of iron around South Georgia, Southern Ocean: A modelling perspective. *Biogeosciences*, *11*(7), 1981–2001. https://doi.org/10.5194/bg-11-1981-2014

Boss, E., & Pegau, W. S. (2001). Relationship of light scattering at an angle in the backward direction to the backscattering coefficient. *Applied Optics*, *40*(30), 5503–5507. https://doi.org/10.1364/AO.40.005503

Boss, E., Slade, W., & Hill, P. (2009). Effect of particulate aggregation in aquatic environments on the beam attenuation and its utility as a proxy for particulate mass. *Optics Express*, *17*(11), 9408–9420. https://doi.org/10.1364/OE.17.009408

Bowie, A. R., van der Merwe, P., Quéroué, F., Trull, T., Fourquez, M., Planchon, F., et al. (2015). Iron budgets for three distinct biogeochemical sites around the Kerguelen Archipelago (Southern Ocean) during the natural fertilisation study, KEOPS-2. *Biogeosciences*, *12*(14), 4421–4445. https://doi.org/10.5194/bg-12-4421-2015

Boyd, P. W., Claustre, H., Levy, M., Siegel, D. A., & Weber, T. (2019). Multi-faceted particle pumps drive carbon sequestration in the ocean. *Nature*, *568*(7752), 327–335. https://doi.org/10.1038/s41586-019-1098-2

Briggs, E. M., Martz, T. R., Talley, L. D., Mazloff, M. R., & Johnson, K. S. (2018). Physical and biological drivers of biogeochemical tracers within the seasonal sea ice zone of the southern ocean from profiling floats. *Journal of Geophysical Research: Oceans*, *123*(2), 746–758. https://doi.org/10.1002/2017JC012846

Briggs, N., DallOlmo, G., & Claustre, H. (2020). Major role of particle fragmentation in regulating biological sequestration of CO_2 by the oceans. *Science*, *367*(6479), 791–793. https://doi.org/10.1126/science.aay1790

Briggs, N., Perry, M. J., Cetinić, I., Lee, C., D'Asaro, E., Gray, A. M., & Rehm, E. (2011). High-resolution observations of aggregate flux during a sub-polar North Atlantic spring bloom. *Deep-Sea Research Part I Oceanographic Research Papers*, *58*(10), 1031–1039. https://doi.org/10.1016/j.dsr.2011.07.007

Briggs, N. T., Slade, W. H., Boss, E., & Perry, M. J. (2013). Method for estimating mean particle size from high-frequency fluctuations in beam attenuation or scattering measurements. *Applied Optics*, *52*(27), 6710–6725. https://doi.org/10.1364/AO.52.006710

Buesseler, K. O., & Boyd, P. W. (2009). Shedding light on processes that control particle export and flux attenuation in the twilight zone of the open ocean. *Limnology & Oceanography*, *54*(4), 1210–1232. https://doi.org/10.4319/lo.2009.54.4.1210

Buesseler, K. O., Boyd, P. W., Black, E. E., & Siegel, D. A. (2020). Metrics that matter for assessing the ocean biological carbon pump. *Proceedings of the National Academy of Sciences of the United of States America*, *117*(18), 9679–9687. https://doi.org/10.1073/pnas.1918114117

Cael, B. B., Cavan, E. L., & Britten, G. L. (2021). Reconciling the size-dependence of marine particle sinking speed. *Geophysical Research Letters*, *48*(5), e2020GL091771. https://doi.org/10.1029/2020GL091771

Carlotti, F., Jouandet, M.-P., Nowaczyk, A., Harmelin-Vivien, M., Lefèvre, D., Richard, P., et al. (2015). Mesozooplankton structure and functioning during the onset of the Kerguelen phytoplankton bloom during the KEOPS2 survey. *Biogeosciences*, *12*(14), 4543–4563. https://doi.org/10.5194/bg-12-4543-2015

Cavan, E. L., Belcher, A., Atkinson, A., Hill, S. L., Kawaguchi, S., McCormack, S., et al. (2019). The importance of Antarctic krill in biogeochemical cycles. *Nature Communications*, *10*(1), 4742. https://doi.org/10.1038/s41467-019-12668-7

Cavan, E. L., Henson, S. A., Belcher, A., & Sanders, R. (2017). Role of zooplankton in determining the efficiency of the biological carbon pump. *Biogeosciences*, *14*(1), 177–186. https://doi.org/10.5194/bg-14-177-2017

Cavan, E. L., le Moigne, F. A. C., Poulton, A. J., Tarling, G. A., Ward, P., Daniels, C. J., et al. (2015). Attenuation of particulate organic carbon flux in the Scotia Sea, Southern Ocean, is controlled by zooplankton fecal pellets. *Geophysical Research Letters*, *42*(3), 821–830. https://doi.org/10.1002/2014GL062744

Cetinić, I., Perry, M. J., Briggs, N. T., Kallin, E., D'Asaro, E. A., & Lee, C. M. (2012). Particulate organic carbon and inherent optical properties during 2008 North Atlantic bloom experiment. *Journal of Geophysical Research*, *117*(6), C06028. https://doi.org/10.1029/2011JC007771

Cetinić, I., Perry, M. J., D'Asaro, E., Briggs, N., Poulton, N., Sieracki, M. E., & Lee, C. M. (2015). A simple optical index shows spatial and temporal heterogeneity in phytoplankton community composition during the 2008 North Atlantic Bloom Experiment. *Biogeosciences*, *12*(7), 2179–2194. https://doi.org/10.5194/bg-12-2179-2015

Claustre, H., Johnson, K. S., & Takeshita, Y. (2020). Observing the Global Ocean with biogeochemical-Argo. *Annual Review of Marine Science*, *12*(1), 23–48. https://doi.org/10.1146/annurev-marine-010419

Claustre, H., Legendre, L., Boyd, P. W., & Levy, M. (2021). The Oceans' biological carbon pumps: Framework for a Research observational community approach. *Frontiers in Marine Science*, *8*. https://doi.org/10.3389/fmars.2021.780052

Cornec, M., Claustre, H., Mignot, A., Guidi, L., Lacour, L., Poteau, A., et al. (2021). Deep chlorophyll maxima in the global ocean: Occurrences, drivers and characteristics. *Global Biogeochemical Cycles*, *35*(4), e2020GB006759. https://doi.org/10.1029/2020GB006759

Dall'Olmo, G., & Mork, K. A. (2014). Carbon export by small particles in the Norwegian Sea. *Geophysical Research Letters*, *41*(8), 2921–2927. https://doi.org/10.1002/2014GL059244

Deppeler, S. L., & Davidson, A. T. (2017). Southern Ocean phytoplankton in a changing climate. *Frontiers in Marine Science*, *4*, 40. https://doi.org/10.3389/fmars.2017.00040

DeVries, T. (2014). The oceanic anthropogenic CO_2 sink: Storage, air-sea fluxes, and transports over the industrial era. *Global Biogeochemical Cycles*, *28*(7), 631–647. https://doi.org/10.1002/2013GB004739

d'Ovidio, F., della Penna, A., Trull, T. W., Nencioli, F., Pujol, M.-I., Rio, M.-H., et al. (2015). The biogeochemical structuring role of horizontal stirring: Lagrangian perspectives on iron delivery downstream of the Kerguelen Plateau. *Biogeosciences*, *12*(19), 5567–5581. https://doi.org/10.5194/bg-12-5567-2015

Durkin, C. A., Buesseler, K. O., Cetinić, I., Estapa, M. L., Kelly, R. P., & Omand, M. (2021). A visual tour of carbon export by sinking particles. *Global Biogeochemical Cycles*, *35*(10), e2021GB006985. https://doi.org/10.1029/2021GB006985

Durkin, C. A., Cetinić, I., Estapa, M., Ljubešić, Z., Mucko, M., Neeley, A., & Omand, M. (2022). Tracing the path of carbon export in the ocean though DNA sequencing of individual sinking particles. *The ISME Journal*, *16*(8), 1896–1906. https://doi.org/10.1038/s41396-022-01239-2

Ebersbach, F., & Trull, T. W. (2008). Sinking particle properties from polyacrylamide gels during the KErguelen Ocean and Plateau compared Study (KEOPS): Zooplankton control of carbon export in an area of persistent natural iron inputs in the Southern Ocean. *Limnology & Oceanography*, *53*(1), 212–224. https://doi.org/10.4319/lo.2008.53.1.0212

Ebersbach, F., Trull, T. W., Davies, D. M., & Bray, S. G. (2011). Controls on mesopelagic particle fluxes in the sub-Antarctic and polar frontal zones in the Southern Ocean South of Australia in summer—Perspectives from free-drifting sediment traps. *Deep Sea Research Part II: Topical Studies in Oceanography*, *58*(21), 2260–2276. https://doi.org/10.1016/j.dsr2.2011.05.025

Estapa, M., Durkin, C., Buesseler, K., Johnson, R., & Feen, M. (2017). Carbon flux from bio-optical profiling floats: Calibrating transmissometers for use as optical sediment traps. *Deep-Sea Research Part I Oceanographic Research Papers*, *120*, 100–111. https://doi.org/10.1016/j.dsr.2016.12.003

Estapa, M., Durkin, C., Slade, W., Huffard, C., O'Neill, S., & Omand, M. (2023). A new, global optical sediment trap calibration. *EarthArXiv*. https://doi.org/10.31223/X5NQ1X

Estapa, M. L., Buesseler, K., Boss, E., & Gerbi, G. (2013). Autonomous, high-resolution observations of particle flux in the oligotrophic ocean. *Biogeosciences*, *10*(8), 5517–5531. https://doi.org/10.5194/bg-10-5517-2013

Estapa, M. L., Feen, M. L., & Breves, E. (2019). Direct observations of biological carbon export from profiling floats in the subtropical North Atlantic. *Global Biogeochemical Cycles*, *33*(3), 282–300. https://doi.org/10.1029/2018GB006098

Gardner, W. D., Richardson, M. J., & Smith, W. O. (2000). Seasonal patterns of water column particulate organic carbon and fluxes in the Ross Sea, Antarctica. *Deep Sea Research Part II: Topical Studies in Oceanography*, *47*(15), 3423–3449. https://doi.org/10.1016/S0967-0645(00)00074-6

Garrity, C., Ramseier, R. O., Peinert, R., Kern, S., & Fischer, G. (2005). Water column particulate organic carbon modeled fluxes in the ice-frequented Southern Ocean. *Journal of Marine Systems*, *56*(1), 133–149. https://doi.org/10.1016/j.jmarsys.2004.09.009

Gohin, F., Druon, J. N., & Lampert, L. (2002). A five channel chlorophyll concentration algorithm applied to SeaWiFS data processed by SeaDAS in coastal waters. *International Journal of Remote Sensing*, *23*(8), 1639–1661. https://doi.org/10.1080/01431160110071879

Gray, A. R., Johnson, K. S., Bushinsky, S. M., Riser, S. C., Russell, J. L., Talley, L. D., et al. (2018). Autonomous biogeochemical floats detect significant carbon dioxide outgassing in the high-latitude Southern Ocean. *Geophysical Research Letters*, *45*(17), 9049–9057. https://doi.org/10.1029/2018GL078013

Guidi, L., Jackson, G. A., Stemmann, L., Miquel, J. C., Picheral, M., & Gorsky, G. (2008). Relationship between particle size distribution and flux in the mesopelagic zone. *Deep Sea Research Part I: Oceanographic Research Papers*, *55*(10), 1364–1374. https://doi.org/10.1016/j.dsr.2008.05.014

Guidi, L., Legendre, L., Reygondeau, G., Uitz, J., Stemmann, L., & Henson, S. A. (2015). A new look at ocean carbon remineralization for estimating deepwater sequestration. *Global Biogeochemical Cycles*, *29*(7), 1044–1059. https://doi.org/10.1002/2014GB005063

Guinehut, S., Dhomps, A.-L., Larnicol, G., & le Traon, P.-Y. (2012). High resolution 3-D temperature and salinity fields derived from in situ and satellite observations. *Ocean Science*, *8*(5), 845–857. https://doi.org/10.5194/os-8-845-2012

Haëntjens, N., Della Penna, A., Briggs, N., Karp-Boss, L., Gaube, P., Claustre, H., & Boss, E. (2020). Detecting mesopelagic organisms using biogeochemical-Argo floats. *Geophysical Research Letters*, *47*(6), e2019GL086088. https://doi.org/10.1029/2019GL086088

Halfter, S., Cavan, E. L., Swadling, K. M., Eriksen, R. S., & Boyd, P. W. (2020). The role of zooplankton in establishing carbon export regimes in the southern ocean—A comparison of two representative case studies in the subantarctic region. *Frontiers in Marine Science*, *7*, 837. https://doi.org/10.3389/fmars.2020.567917

Henson, S. A., Sanders, R., & Madsen, E. (2012). Global patterns in efficiency of particulate organic carbon export and transfer to the deep ocean. *Global Biogeochemical Cycles*, *26*(1), GB1028. https://doi.org/10.1029/2011GB004099

Holte, J., & Talley, L. (2009). A new algorithm for finding mixed layer depths with applications to Argo data and subantarctic mode water formation. *Journal of Atmospheric and Oceanic Technology*, *26*(9), 1920–1939. https://doi.org/10.1175/2009JTECHO543.1.s1

Holte, J., Talley, L. D., Gilson, J., & Roemmich, D. (2017). An Argo mixed layer climatology and database. *Geophysical Research Letters*, *44*(11), 5618–5626. https://doi.org/10.1002/2017GL073426

Hu, C., Lee, Z., & Franz, B. (2012). Chlorophyll a algorithms for oligotrophic oceans: A novel approach based on three-band reflectance difference. *Journal of Geophysical Research*, *117*(1), C01011. https://doi.org/10.1029/2011JC007395

Huisman, J., & Sommeijer, B. (2002). Maximal sustainable sinking velocity of phytoplankton. *Marine Ecology Progress Series*, *244*, 39–48. https://doi.org/10.3354/meps244039

Iversen, M. H., Nowald, N., Ploug, H., Jackson, G. A., & Fischer, G. (2010). High resolution profiles of vertical particulate organic matter export off Cape Blanc, Mauritania: Degradation processes and ballasting effects. *Deep Sea Research Part I: Oceanographic Research Papers*, *57*(6), 771–784. https://doi.org/10.1016/j.dsr.2010.03.007

Iversen, M. H., & Ploug, H. (2013). Temperature effects on carbon-specific respiration rate and sinking velocity of diatom aggregates—Potential implications for Deep Ocean export processes. *Biogeosciences*, *10*(6), 4073–4085. https://doi.org/10.5194/bg-10-4073-2013

Johnson, K. S., Plant, J. N., Dunne, J. P., Talley, L. D., & Sarmiento, J. L. (2017). Annual nitrate drawdown observed by SOCCOM profiling floats and the relationship to annual net community production. *Journal of Geophysical Research: Oceans*, *122*(8), 6668–6683. https://doi.org/10.1002/2017JC012839

Jouandet, M.-P., Jackson, G. A., Carlotti, F., Picheral, M., Stemmann, L., & Blain, S. (2014). Rapid formation of large aggregates during the spring bloom of Kerguelen island: Observations and model comparisons. *Biogeosciences*, *11*(16), 4393–4406. https://doi.org/10.5194/bg-11-4393-2014

Kemp, A. E. S., Pike, J., Pearce, R. B., & Lange, C. B. (2000). The "fall dump"—A new perspective on the role of a "shade flora" in the annual cycle of diatom production and export flux. *Deep Sea Research Part II: Topical Studies in Oceanography*, *47*(9), 2129–2154. https://doi.org/10.1016/S0967-0645(00)00019-9

Kheireddine, M., Dall'Olmo, G., Ouhssain, M., Krokos, G., Claustre, H., Schmechtig, C., et al. (2020). Organic carbon export and loss rates in the red sea. *Global Biogeochemical Cycles*, *34*(10), e2020GB006650. https://doi.org/10.1029/2020GB006650

Kim, M., Hwang, J., Kim, H. J., Kim, D., Yang, E. J., Ducklow, H. W., et al. (2015). Sinking particle flux in the sea ice zone of the Amundsen Shelf, Antarctica. *Deep Sea Research Part I: Oceanographic Research Papers*, *101*, 110–117. https://doi.org/10.1016/j.dsr.2015.04.002

Lacour, L., Briggs, N., Claustre, H., Ardyna, M., & Dall'Olmo, G. (2019). The intraseasonal dynamics of the mixed layer pump in the subpolar North Atlantic Ocean: A biogeochemical-Argo float approach. *Global Biogeochemical Cycles*, *33*(3), 266–281. https://doi.org/10.1029/2018GB005997

Lafond, A., Leblanc, K., Legras, J., Cornet, V., & Quéguiner, B. (2020). The structure of diatom communities constrains biogeochemical properties in surface waters of the Southern Ocean (Kerguelen Plateau). *Journal of Marine Systems*, *212*, 103458. https://doi.org/10.1016/j.jmarsys.2020.103458

Lancelot, C., de Montety, A., Goosse, H., Becquevort, S., Schoemann, V., Pasquer, B., & Vancoppenolle, M. (2009). Spatial distribution of the iron supply to phytoplankton in the Southern Ocean: A model study. *Biogeosciences*, *6*(12), 2861–2878. https://doi.org/10.5194/bg-6-2861-2009

Lasbleiz, M., Leblanc, K., Armand, L. K., Christaki, U., Georges, C., Obernosterer, I., & Quéguiner, B. (2016). Composition of diatom communities and their contribution to plankton biomass in the naturally iron-fertilized region of Kerguelen in the Southern Ocean. *FEMS Microbiology Ecology*, *92*(11), fiw171. https://doi.org/10.1093/femsec/fiw171

Laurenceau-Cornec, E. C., Trull, T. W., Davies, D. M., Bray, S. G., Doran, J., Planchon, F., et al. (2015). The relative importance of phytoplankton aggregates and zooplankton fecal pellets to carbon export: Insights from free-drifting sediment trap deployments in naturally iron-fertilised waters near the Kerguelen Plateau. *Biogeosciences*, *12*(4), 1007–1027. https://doi.org/10.5194/bg-12-1007-2015

Legendre, L., & Le Fèvre, L. F. (1995). Microbial food webs and the export of biogenic carbon in oceans. *Aquatic Microbial Ecology*, *09*(1), 69–77. https://doi.org/10.3354/ame009069

Leys, C., Ley, C., Klein, O., Bernard, P., & Licata, L. (2013). Detecting outliers: Do not use standard deviation around the mean, use absolute deviation around the median. *Journal of Experimental Social Psychology*, *49*(4), 764–766. https://doi.org/10.1016/j.jesp.2013.03.013

Llort, J., Langlais, C., Matear, R., Moreau, S., Lenton, A., & Strutton, P. G. (2018). Evaluating Southern Ocean carbon eddy-pump from biogeochemical-Argo floats. *Journal of Geophysical Research: Oceans*, *123*(2), 971–984. https://doi.org/10.1002/2017JC012861

MacCready, P., & Quay, P. (2001). Biological export flux in the Southern Ocean estimated from a climatological nitrate budget. *Deep Sea Research Part II: Topical Studies in Oceanography*, *48*(19), 4299–4322. https://doi.org/10.1016/S0967-0645(01)00090-X

Marsay, C. M., Sanders, R. J., Henson, S. A., Pabortsava, K., Achterberg, E. P., & Lampitt, R. S. (2015). Attenuation of sinking particulate organic carbon flux through the mesopelagic ocean. *Proceedings of the National Academy of Sciences of the United States of America*, *112*(4), 1089–1094. https://doi.org/10.1073/pnas.1415311112

Martin, J. H., Gordon, R. M., & Fitzwater, S. E. (1990). Iron in Antarctic waters. *Nature*, *345*(6271), 156–158. https://doi.org/10.1038/345156a0

McKenzie, T., Twardowski, M., Briggs, N., Nayak, A. R., Boswell, K. M., & Dalgleish, F. (2020). Three-dimensional imaging lidar for characterizing particle fields and organisms in the mesopelagic zone. *Frontiers in Marine Science*, *7*. https://doi.org/10.3389/fmars.2020.558745

Morel, A., Huot, Y., Gentili, B., Werdell, P. J., Hooker, S. B., & Franz, B. A. (2007). Examining the consistency of products derived from various ocean color sensors in open ocean (Case 1) waters in the perspective of a multi-sensor approach. *Remote Sensing of Environment*, *111*(1), 69–88. https://doi.org/10.1016/j.rse.2007.03.012

Mouw, C. B., Barnett, A., McKinley, G. A., Gloege, L., & Pilcher, D. (2016a). Phytoplankton size impact on export flux in the global ocean. *Global Biogeochemical Cycles*, *30*(10), 1542–1562. https://doi.org/10.1002/2015GB005355

Mouw, C. B., Barnett, A., McKinley, G. A., Gloege, L., & Pilcher, D. (2016b). Global ocean particulate organic carbon flux merged with satellite parameters. *Earth System Science Data*, *8*(2), 531–541. https://doi.org/10.5194/essd-8-531-2016

Mulet, S., Rio, M.-H., Mignot, A., Guinehut, S., & Morrow, R. (2012). A new estimate of the global 3D geostrophic ocean circulation based on satellite data and in-situ measurements. *Deep Sea Research Part II: Topical Studies in Oceanography*, *77–80*, 70–81. https://doi.org/10.1016/j.dsr2.2012.04.012

Neukermans, G., Bach, L. T., Butterley, A., Sun, Q., Claustre, H., & Fournier, G. R. (2023). Quantitative and mechanistic understanding of the open ocean carbonate pump - Perspectives for remote sensing and autonomous in situ observation. *Earth-Science Reviews*, *239*, 104359. https://doi.org/10.1016/j.earscirev.2023.104359

Neukermans, G., Loisel, H., Mériaux, X., Astoreca, R., & McKee, D. (2012). In situ variability of mass-specific beam attenuation and backscattering of marine particles with respect to particle size, density, and composition. *Limnology & Oceanography*, *57*(1), 124–144. https://doi.org/10.4319/lo.2012.57.1.0124

Nielsdóttir, M. C., Bibby, T. S., Moore, C. M., Hinz, D. J., Sanders, R., Whitehouse, M., et al. (2012). Seasonal and spatial dynamics of iron availability in the Scotia Sea. *Marine Chemistry*, *130–131*, 62–72. https://doi.org/10.1016/j.marchem.2011.12.004

Omand, M. M., Govindarajan, R., He, J., & Mahadevan, A. (2020). Sinking flux of particulate organic matter in the oceans: Sensitivity to particle characteristics. *Scientific Reports*, *10*(1), 5582. https://doi.org/10.1038/s41598-020-60424-5

O'Reilly, J. E., Maritorena, S., Mitchell, B. G., Siegel, D. A., Carder, K. L., Garver, S. A., et al. (1998). Ocean color chlorophyll algorithms for SeaWiFS. *Journal of Geophysical Research*, *103*(C11), 24937–24953. https://doi.org/10.1029/98JC02160

O'Reilly, J. E., Maritorena, S., Siegel, D. A., O'brien, M. C., Toole, D., Mitchell, B. G., et al. (2000). Ocean color chlorophyll-a algorithms for SeaWiFS, OC2, and OC4: Version 4. *SeaWIFS Postlaunch Technical Report Series*, *11*(3), 9–23.

Organelli, E., Barbieux, M., Claustre, H., Schmechtig, C., Poteau, A., Bricaud, A., et al. (2017). Two databases derived from BGC-Argo float measurements for marine biogeochemical and bio-optical applications. *Earth System Science Data*, *9*(2), 861–880. https://doi.org/10.5194/essd-9-861-2017

Organelli, E., Claustre, H., Bricaud, A., Schmechtig, C., Poteau, A., Xing, X., et al. (2016). A novel near-real-time quality-control procedure for radiometric profiles measured by bio-argo floats: Protocols and performances. *Journal of Atmospheric and Oceanic Technology*, *33*(5), 937–951. https://doi.org/10.1175/JTECH-D-15-0193.1

Pauli, N.-C., Flintrop, C. M., Konrad, C., Pakhomov, E. A., Swoboda, S., Koch, F., et al. (2021). Krill and salp faecal pellets contribute equally to the carbon flux at the Antarctic Peninsula. *Nature Communications*, *12*(1), 7168. https://doi.org/10.1038/s41467-021-27436-9

Person, R., Vancoppenolle, M., Aumont, O., & Malsang, M. (2021). Continental and sea ice iron sources fertilize the southern ocean in synergy. *Geophysical Research Letters*, *48*(23), e2021GL094761. https://doi.org/10.1029/2021GL094761

Picheral, M., Catalano, C., Brousseau, D., Claustre, H., Coppola, L., Leymarie, E., et al. (2022). The underwater vision profiler 6: An imaging sensor of particle size spectra and plankton, for autonomous and cabled platforms. *Limnology and Oceanography: Methods*, *20*(2), 115–129. https://doi.org/10.1002/lom3.10475

Planchon, F., Ballas, D., Cavagna, A.-J., Bowie, A. R., Davies, D., Trull, T., et al. (2015). Carbon export in the naturally iron-fertilized Kerguelen area of the Southern Ocean based on the ^234Th approach. *Biogeosciences*, *12*(12), 3831–3848. https://doi.org/10.5194/bg-12-3831-2015

Ploug, H., Iversen, M. H., Koski, M., & Buitenhuis, E. T. (2008). Production, oxygen respiration rates, and sinking velocity of copepod fecal pellets: Direct measurements of ballasting by opal and calcite. *Limnology & Oceanography*, *53*(2), 469–476. https://doi.org/10.4319/lo.2008.53.2.0469

Puigcorbé, V., Roca-Martí, M., Masqué, P., Benitez-Nelson, C. R., Rutgers, V. D., Loeff, M., et al. (2017). Particulate organic carbon export across the Antarctic circumpolar current at 10°E: Differences between north and South of the Antarctic polar front. *Deep Sea Research Part II: Topical Studies in Oceanography*, *138*, 86–101. https://doi.org/10.1016/j.dsr2.2016.05.016

R Core Team. (2022). R: A language and environment for statistical computing. Retrieved from https://www.R-project.org/

Rembauville, M., Blain, S., Armand, L., Quéguiner, B., & Salter, I. (2015). Export fluxes in a naturally iron-fertilized area of the Southern Ocean—Part 2: Importance of diatom resting spores and faecal pellets for export. *Biogeosciences*, *12*(11), 3171–3195. https://doi.org/10.5194/bg-12-3171-2015

Rembauville, M., Briggs, N., Ardyna, M., Uitz, J., Catala, P., Penkerc'h, C., et al. (2017). Plankton assemblage estimated with BGC-Argo floats in the Southern Ocean: Implications for seasonal successions and particle export. *Journal of Geophysical Research: Oceans*, *122*(10), 8278–8292. https://doi.org/10.1002/2017JC013067

Rembauville, M., Salter, I., Dehairs, F., Miquel, J.-C., & Blain, S. (2018). Annual particulate matter and diatom export in a high nutrient, low chlorophyll area of the Southern Ocean. *Polar Biology*, *41*(1), 25–40. https://doi.org/10.1007/s00300-017-2167-3

Rembauville, M., Salter, I., Leblond, N., Gueneugues, A., & Blain, S. (2015). Export fluxes in a naturally iron-fertilized area of the Southern Ocean—Part 1: Seasonal dynamics of particulate organic carbon export from a moored sediment trap. *Biogeosciences*, *12*(11), 3153–3170. https://doi.org/10.5194/bg-12-3153-2015

Rohr, T., Long, M. C., Kavanaugh, M. T., Lindsay, K., & Doney, S. C. (2017). Variability in the mechanisms controlling Southern Ocean phytoplankton bloom phenology in an ocean model and satellite observations. *Global Biogeochemical Cycles*, *31*(5), 922–940. https://doi.org/10.1002/2016GB005615

Rosengard, S. Z., Lam, P. J., Balch, W. M., Auro, M. E., Pike, S., Drapeau, D., & Bowler, B. (2015). Carbon export and transfer to depth across the Southern Ocean great calcite belt. *Biogeosciences*, *12*(13), 3953–3971. https://doi.org/10.5194/bg-12-3953-2015

RStudio Team. (2022). *RStudio*. Integrated Development Environment for R. Retrieved from http://www.rstudio.com/

Sabu, P., Anilkumar, N., George, J. v., Chacko, R., Tripathy, S. C., & Achuthankutty, C. T. (2014). The influence of air–sea–ice interactions on an anomalous phytoplankton bloom in the Indian Ocean sector of the Antarctic Zone of the Southern Ocean during the austral summer, 2011. *Polar Science*, *8*(4), 370–384. https://doi.org/10.1016/j.polar.2014.08.001

Salter, I., Kemp, A. E. S., Moore, C. M., Lampitt, R. S., Wolff, G. A., & Holtvoeth, J. (2012). Diatom resting spore ecology drives enhanced carbon export from a naturally iron-fertilized bloom in the Southern Ocean. *Global Biogeochemical Cycles*, *26*(1). https://doi.org/10.1029/2010GB003977

Sarmiento, J. L., & Gruber, N. (2006). Ocean biogeochemical dynamics: xiii + 503. In *Geological magazine*. Princeton University Press. Price £48.95 (hard covers). 0 691 01707 7. https://doi.org/10.1017/S0016756807003755

Sauzède, R., Bittig, H. C., Claustre, H., de Fommervault, O., Gattuso, J.-P., Legendre, L., & Johnson, K. S. (2017). Estimates of water-column nutrient concentrations and carbonate system parameters in the global ocean: A novel approach based on neural networks. *Frontiers in Marine Science*, *4*. https://doi.org/10.3389/fmars.2017.00128

Sauzède, R., Claustre, H., Uitz, J., Jamet, C., Dall'Olmo, G., D'Ortenzio, F., et al. (2016). A neural network-based method for merging ocean color and Argo data to extend surface bio-optical properties to depth: Retrieval of the particulate backscattering coefficient. *Journal of Geophysical Research: Oceans*, *121*(4), 2552–2571. https://doi.org/10.1002/2015JC011408

Schmechtig, C., Poteau, A., Claustre, H., D'Ortenzio, F., Dall'Olmo, G., & Boss, E. (2018). Processing Bio-Argo particle backscattering at the DAC level. https://doi.org/10.13155/39459

Schmechtig, C., Poteau, A., Claustre, H., D'Ortenzio, F., & Emmanuel, B. (2015). Processing Bio-Argo chlorophyll-a concentration at the DAC level Argo data management Processing Bio-Argo chlorophyll-a concentration at the DAC level. https://doi.org/10.13155/39468

Sergi, S., Baudena, A., Cotté, C., Ardyna, M., Blain, S., & d'Ovidio, F. (2020). Interaction of the Antarctic Circumpolar current with seamounts fuels moderate blooms but vast foraging grounds for multiple marine predators. *Frontiers in Marine Science*, *7*. https://doi.org/10.3389/fmars.2020.00416

Siegel, D. A., Buesseler, K. O., Behrenfeld, M. J., Benitez-Nelson, C. R., Boss, E., Brzezinski, M. A., et al. (2016). Prediction of the export and fate of global ocean net primary production: The EXPORTS science plan. *Frontiers in Marine Science*, *3*. https://doi.org/10.3389/fmars.2016.00022

Siegel, D. A., DeVries, T., Doney, S. C., & Bell, T. (2021). Assessing the sequestration time scales of some ocean-based carbon dioxide reduction strategies. *Environmental Research Letters*, *16*(10), 104003. https://doi.org/10.1088/1748-9326/ac0be0

Slade, W. H., Boss, E., & Russo, C. (2011). Effects of particle aggregation and disaggregation on their inherent optical properties. *Optics Express*, *19*(9), 7945–7959. https://doi.org/10.1364/OE.19.007945

Stukel, M. R., Song, H., Goericke, R., & Miller, A. J. (2018). The role of subduction and gravitational sinking in particle export, carbon sequestration, and the remineralization length scale in the California Current Ecosystem. *Limnology & Oceanography*, *63*(1), 363–383. https://doi.org/10.1002/lno.10636

Su, J., Schallenberg, C., Rohr, T., Strutton, P. G., & Phillips, H. E. (2022). New estimates of southern ocean annual net community production revealed by BGC-Argo floats. *Geophysical Research Letters*, *49*(15), e2021GL097372. https://doi.org/10.1029/2021GL097372

Takeda, S. (1998). Influence of iron availability on nutrient consumption ratio of diatoms in oceanic waters. *Nature*, *393*(6687), 774–777. https://doi.org/10.1038/31674

Terrats, L., Claustre, H., Briggs, N., Poteau, A., Briat, B., Lacour, L., et al. (2023). BioGeoChemical-Argo float data including bio-optical profiles and POC flux at 1000m in the Southern Ocean from 2014 to 2019.

Terrats, L., Claustre, H., Cornec, M., Mangin, A., & Neukermans, G. (2020). Detection of coccolithophore blooms with BioGeoChemical-Argo floats. *Geophysical Research Letters*, *47*(23), e2020GL090559. https://doi.org/10.1029/2020GL090559

Thierry, V., & Bittig, H. (2021). Argo quality control manual for dissolved oxygen concentration. https://doi.org/10.13155/46542

Thomalla, S. J., Ogunkoya, A. G., Vichi, M., & Swart, S. (2017). Using optical sensors on gliders to estimate phytoplankton carbon concentrations and chlorophyll-to-carbon ratios in the southern ocean. *Frontiers in Marine Science*, *4*. https://doi.org/10.3389/fmars.2017.00034

Tréguer, P., Bowler, C., Moriceau, B., Dutkiewicz, S., Gehlen, M., Aumont, O., et al. (2018). Influence of diatom diversity on the ocean biological carbon pump. *Nature Geoscience*, *11*(1), 27–37. https://doi.org/10.1038/s41561-017-0028-x

Trull, T. W., Bray, S. G., Manganini, S. J., Honjo, S., & François, R. (2001). Moored sediment trap measurements of carbon export in the Subantarctic and Polar Frontal zones of the Southern Ocean, south of Australia. *Journal of Geophysical Research*, *106*(C12), 31489–31509. https://doi.org/10.1029/2000JC000308

Viljoen, J. J., Philibert, R., van Horsten, N., Mtshali, T., Roychoudhury, A. N., Thomalla, S., & Fietz, S. (2018). Phytoplankton response in growth, photophysiology and community structure to iron and light in the Polar Frontal Zone and Antarctic waters. *Deep Sea Research Part I: Oceanographic Research Papers*, *141*, 118–129. https://doi.org/10.1016/j.dsr.2018.09.006

Waite, A., Fisher, A., Thompson, P. A., & Harrison, P. J. (1997). Sinking rate versus cell volume relationships illuminate sinking rate control mechanisms in marine diatoms. *Marine Ecology Progress Series*, *157*, 97–108. https://doi.org/10.3354/meps157097

Wiedmann, I., Ceballos-Romero, E., Villa-Alfageme, M., Renner, A. H. H., Dybwad, C., van der Jagt, H., et al. (2020). Arctic observations identify phytoplankton community composition as driver of carbon flux attenuation. *Geophysical Research Letters*, *47*(14), e2020GL087465. https://doi.org/10.1029/2020GL087465

Williams, J. R., & Giering, S. L. C. (2022). In situ particle measurements deemphasize the role of size in governing the sinking velocity of marine particles. *Geophysical Research Letters*, *49*(21), e2022GL099563. https://doi.org/10.1029/2022GL099563

Wong, A., Keeley, R., & Carval, T. (2022). Argo quality control manual for CTD and trajectory data. https://doi.org/10.13155/33951

Wynn-Edwards, C. A., Shadwick, E. H., Davies, D. M., Bray, S. G., Jansen, P., Trinh, R., & Trull, T. W. (2020). Particle fluxes at the Australian Southern Ocean time series (SOTS) achieve organic carbon sequestration at rates close to the global median, are dominated by biogenic carbonates, and show No temporal trends over 20-years. *Frontiers in Earth Science*, *8*, 329. https://doi.org/10.3389/feart.2020.00329

Xi, H., Losa, S. N., Mangin, A., Soppa, M. A., Garnesson, P., Demaria, J., et al. (2020). Global retrieval of phytoplankton functional types based on empirical orthogonal functions using CMEMS GlobColour merged products and further extension to OLCI data. *Remote Sensing of Environment*, *240*, 111704. https://doi.org/10.1016/j.rse.2020.111704

Xing, X., Briggs, N., Boss, E., & Claustre, H. (2018). Improved correction for non-photochemical quenching of in situ chlorophyll fluorescence based on a synchronous irradiance profile. *Optics Express*, *26*(19), 24734. https://doi.org/10.1364/oe.26.024734

Zhang, X., Leymarie, E., Boss, E., & Hu, L. (2021). Deriving the angular response function for backscattering sensors. *Applied Optics*, *60*(28), 8676–8687. https://doi.org/10.1364/AO.437735